Fuel 254 (2019) 115681

Contents lists available at ScienceDirect

Fuel

journal homepage: www.elsevier.com/locate/fuel

Full Length Article

# The role of Pt loading on $La_2O_3$-$Al_2O_3$ support for methane conversion reactions via partial oxidation and steam reforming

Jesuina C.S. Araújo[a], Lais F. Oton[b], Bruno Bessa[b], Antonio B.S. Neto[b], Alcineia C. Oliveira[b,*], Rossano Lang[c], Larissa Otubo[d], José M.C. Bueno[e]

[a] Universidade Federal do Espirito Santo, Centro Universitário Norte do Espírito Santo, São Mateus, Espírito Santo, Brazil
[b] Universidade Federal do Ceará, Campus do Pici – Bloco 940, Departamento de Química Analítica e Físico-Química, Fortaleza, Ceará, Brazil
[c] Instituto de Ciência e Tecnologia – ICT, Universidade Federal de São Paulo – UNIFESP, 12231-280 São José dos Campos, São Paulo, Brazil
[d] Centro de Ciência e Tecnologia de Materiais – CCTM, Instituto de Pesquisas Energéticas e Nucleares – IPEN, 05508-000 São Paulo, São Paulo, Brazil
[e] Universidade Federal de São Carlos, C.P. 676, 13565-905, São Carlos, São Paulo, Brazil

## GRAPHICAL ABSTRACT

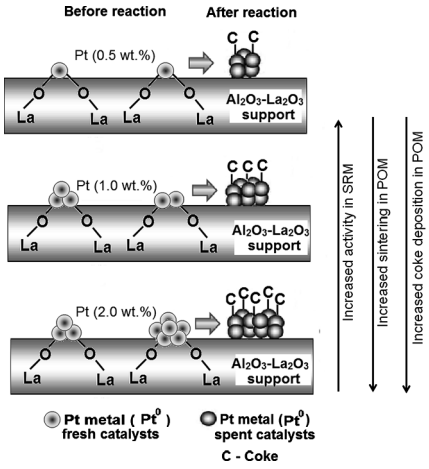


## ARTICLE INFO

*Keywords:*
Pt surface species
Nanoparticles
Partial oxidation of methane
Steam reforming
$La_2O_3$-$Al_2O_3$-supported Pt
Pt loadings

## ABSTRACT

The effects of Pt loadings on the catalytic performance of the $La_2O_3$-$Al_2O_3$-supported Pt nanoparticles are investigated during the partial oxidation (POM) and steam reforming of methane (SRM). From analyses of XRD, UV–Vis, TPR, CO-DRIFTS, XPS, Raman spectroscopy, cyclohexane dehydrogenation reaction, Pt surface species and their dispersions were dully observed. The good degrees of interaction between Pt nanoparticles and lanthana species in the support gave robust catalysts in POM, evidenced by XPS and TEM for low Pt loadings. Arrhenius plots for SRM showed an apparent activation energy of 70 kJ mol$^{-1}$ for all Pt($x$ wt%)/$Al_2O_3$-$La_2O_3$ catalysts. An enrichment of the Pt species at loadings superior to 0.5 wt% resulted in Pt nanoparticles weakly interacting with the $La_2O_3$-$Al_2O_3$ support and the consequent sintering of the particles in SRM and POM reactions. On the contrary, best catalytic results and a more stable performance during POM in 24 h on stream was observed, when dispersing a 0.5 wt% of Pt on the support. A strong interaction between the $PtO_x$ species and the support was crucial for $La_2O_3$ preserve the high dispersion of the Pt entities. This favored the reactivity of surface oxygen species coming from $LaPtO_x[Pt^o]_n$. Indeed, this chemical entity was located on the surface of the solid, at

* Corresponding author.
*E-mail address:* alcineia@ufc.br (A.C. Oliveira).

https://doi.org/10.1016/j.fuel.2019.115681
Received 30 April 2019; Received in revised form 6 June 2019; Accepted 18 June 2019

the periphery of $Pt^o$ particles, being further converted into $La_2PtO_{x[}Pt^o]_{n-1}$. The decomposition of $CH_4$ to CO and $H_2$ as well as the coke gasification on the accessible Pt sites gave better conversions for Pt(0.5 wt%)/$Al_2O_3$-$La_2O_3$ compared with the other solids with higher Pt loadings.

## 1. Introduction

Methane transformations have been the focus of intensive research over the past decades with a rapid expansion of the catalytic reactions to convert this hydrocarbon [1–5]. Of these, steam (SRM), dry reforming (DRM), partial oxidation (POM), autothermal reforming (ATM) and the newest catalytic routes of bi and tri-reforming of methane into syngas are particularly attractive [4–8]. Targeting environmental protection by decrease of methane emissions to avoid the global warming, it is imperative to find alternative catalytic routes to convert methane to valuable compounds [1,4].

Although there have been improved efforts in the routes to transform methane via reforming reactions [4,5,9–11], these approaches are only effective in making use of an efficient catalyst to these reactions. In this sense, a variety of solids, including transition metals such as Ni and Co and noble metals i.e., Pt, Ru, Pd, Rh and Ir supported catalysts have shown promising, as they demonstrate good performances in the conversion of methane reactions [1–7,10–14]. However, a majority of these solids are not scalable or their practical utilization is rare. Therefore, the catalysts are unlikely to be of commercial importance due to their deactivation by carbon deposition, particles sintering or phase transformations during the methane reforming reactions.

In particular, Pt supported catalysts are extensively studied as these solids are effective in the cleavage of C–H bonds and demonstrate high activity in the reforming reactions [3,15,16]. Especially in the case of POM reaction, the well dispersed Pt particles on alumina, titania, ceria, perovskites and spinel oxides, among other supported catalysts have been effectively tested in the reaction [16–18]. Nevertheless, there are some important issues in the aforesaid catalysts related to the stability, particularly those containing alumina, considering the coking, reoxidation under the POM conditions and the solid-state reaction of the transition metal with the support are taking into account.

Additionally, several efforts have been successfully made to overcome the restricted high-temperature stability of Pt particles on alumina either anchoring them on other metal or with adding a second metal (nonmetal) to the support, besides Pt [17–21].

More recently, it has been reported in our studies that the addition of lanthanide oxides to alumina support has great promise to enhance the catalyst lifetime to avoid coking during methane transformations [15,18]. Concerning the use of Pt/$Al_2O_3$–$La_2O_3$ catalyst under POM conditions, it has been reported that the solid was transformed readily into $[LaPt_xO]Pt^o$-like species achieving a good stability during the catalytic runs [18,22]. Also, both cerium oxygen storage capacity and oxygen vacancies near the Pt particles on Pt/$CeO_2$–$Al_2O_3$ catalysts resulted in similar effects in POM reaction [23,24].

Furthermore, steam reforming of methane (SRM) is an endothermic reaction to produce syngas, which is traditionally carried out over a nanosized metallic phase metal dispersed on supports like $Al_2O_3$ [24]. It is well known from literature reports that lanthana has a basic character and promote the dispersion of nanosized active metal particles [8,24]. Besides, the lanthanum oxides have unique properties contributing to form lanthanum oxycarbonate ($La_2O_2CO_3$) species in the presence of $CO_2$. Consequently, the later species reacts with surface carbonaceous deposits to yield $La_2O_3$ and CO during steam reforming process [8].

Although the addition of lanthana has proven to be efficient to enhance the stability and limit coking of Pt/$Al_2O_3$ and thereby, improving its catalytic performance in POM and SRM reactions, it is essential to study the effects of the Pt particles sizes in the resistibility of lanthana promoting Pt/$Al_2O_3$ in both reactions. Currently, our studies displayed evidence for Pt particle sizes strongly influencing in DRM reaction [15]. However, the lack of knowledge on the effects of Pt particles contribution in POM and SRM reactions can be attributed to challenges in controlling the Pt particle sizes due to their inherent reoxidation of platinum by $O_2$ or steam during POM and SRM runs, respectively.

Thus, the present work investigates the influence of the surface Pt particles and their sizes in the catalytic activity of Pt($x$ wt%)/$Al_2O_3$-$La_2O_3$ catalysts (where $x$ represents the Pt loadings) in POM and SRM reactions. Based on these considerations, the strategies adopted consisted of the lanthana selection as the promoter, since $La_2O_3$ is not readily reducible and it is very effective for alumina stabilization, as well. Therefore, the $Al_2O_3$-$La_2O_3$ support allows for a better Pt stabilization and methane activation in POM and SRM long terms stability runs. This has never been observed experimentally for sol–gel based- Pt ($x$ wt%)/$Al_2O_3$-$La_2O_3$ catalysts, before.

## 2. Experimental

### 2.1. Synthesis of the catalysts

The supported Pt($x$ wt%)/$Al_2O_3$-$La_2O_3$ catalysts were synthesized by a sol–gel method. Details of the method are described elsewhere [18]. In brief, the support was synthesized mixing 103.5 mmol of aluminum tri-*sec*-butoxide (99% Merck) and 3.25 mol of absolute ethanol (99.5% Merck) under vigorous stirring at 100 °C for 1 h. Then, 4.2 mmol of lanthanum nitrate solution was dissolved in the previous mixture and stirred continuously. Afterwards, the suspension was peptized by addition of 25 mL of a nitric acid solution (0.109 mol $L^{-1}$) under stirring. Subsequently, the mixture was refluxed at 100 °C for 14 h to form the $Al_2O_3$-$La_2O_3$ xerogel containing 12 wt% of $La_2O_3$. This support was obtained by calcination of the xerogel at 950 °C for 6 h, using synthetic air flow. The support possessing a 12 wt% of La was denoted as $Al_2O_3$-$La_2O_3$.

Pt($x$ wt%)/$Al_2O_3$-$La_2O_3$ catalysts were prepared through Pt impregnation procedure to incorporate the $H_2PtCl_6{\cdot}6H_2O$ solution (Umicore Brasil) on the aforesaid $Al_2O_3$-$La_2O_3$ support. The abovementioned mixture was stirred in a rotary evaporator at 70 °C. The catalysts were subjected to a drying at 60 °C overnight and finally calcined at 300 °C under air flow.

The solids were labeled as Pt(0.5 wt%)/$Al_2O_3$-$La_2O_3$, Pt(1.0 wt%)/$Al_2O_3$-$La_2O_3$ and Pt(2.0 wt%)/$Al_2O_3$-$La_2O_3$, respectively for 0.5, 1.0 and 2.0 wt% of Pt on the solids. These catalysts were designed as Pt($x$ wt%)/$Al_2O_3$-$La_2O_3$.

### 2.2. Characterization of the catalysts

The crystalline phases were determined by X-ray powder diffraction (XRD) patterns in a Rigaku Multiflex diffractometer using Cu $K_\alpha$ radiation. The diffractograms were collected in the 2$\theta$ region of 5–80° with a 0.02 step-scan and a step time of 2 s. The patterns were recorded and compared with those of the Joint Powder Diffraction Committee files (JCPDS).

The Pt loadings were measured by chemical analyses using inductively coupled plasma optical emission spectroscopy (ICP-OES) in the AtomScan 25 spectrometer (Thermo Jarrel Ash) equipment.

Nitrogen adsorption–desorption isotherms were obtained using a Micromeritics ASAP 2000 equipment. Before the analyses, the samples were outgassed under vacuum at 200 °C for 2 h. The specific area, average pore size and total pore volume of the catalysts were obtained by the BET and BJH methods, respectively.

UV–Vis diffuse reflectance spectra (DRS) were obtained in a Cary 5G UV–Vis-Nir Varian spectrometer.

Temperature-programmed reduction ($H_2$-TPR) experiments were conducted in a Micromeritics Pulse Chemisorb 2705 equipment, which was coupled with a thermal conductivity detector (TCD). Pre-treatments of the samples were performed in $N_2$ at 150 °C for 1 h using 100 mg of the solids. After the temperature was cooled down to 25 °C, the $H_2$-TPR analyses were carried out by heating the solids from 25 to 1000 °C with a ramping rate of 10 °C $min^{-1}$ using a 5% $H_2$/Ar mixture. The effluent gas was analyzed by a thermal conductivity detector (TCD).

The CO adsorption measurements were accompanied by FTIR (CO-DRIFTS) using a Thermo Nicolet 4700 Nexus FT-IR spectrophotometer with MCT detector and Diffuse Reflectance Infrared Fourier Transform Spectroscopy-DRIFTS reactor cell (Spectra Tech). The cell was equipped with $CaF_2$ windows (DRIFT HTHV cell) and connected to a gas-dosing and evacuation system. The spectra were collected with a resolution of 4 $cm^{-1}$ resolution using 64 scans. Before the measurements, the samples were reduced at 650 °C under a 25% $H_2/N_2$ flow for 2 h. The adsorption of CO was performed at 25 °C with CO pulses at a pressure of 20 Torr.

The Scanning Electron Microscopy (SEM) images were taken with a JEOL JSM 6300 microscope operating at 20 kV. The local elemental analysis of the solids was carried out by energy dispersive X-ray analysis (EDS) using an EDAX spectrometer equipped to the SEM microscope.

Transmission electron microscopy (TEM) was used to determine the morphology of particles of the reduced and spent catalysts. The experiments were performed on a JEOL JEM-3010 microscope at an operating voltage of 300 kV and 1.7 Å point resolution. For spent solids, the TEM images were collected using a Jeol JEM 2100 microscope. Prior to the experiments, the samples were dispersed in ethanol or isopropanol and then transferred to carbon coated copper grids.

The average particle size distributions were measured from SEM and TEM images using the Image-Pro Plus software (Media Cybernetics, Inc.). The lognormal density function was used to fit the experimental data of the histograms.

X-ray photoelectron spectra were recorded on VG ESCALAB 200R spectrometer equipped with a hemispherical electron analyzer and an Al $K_\alpha$source ($h\nu$ = 1486.6 eV, 1 eV = 1.6302 × $10^{19}$ J). The binding energy (BE) scale was pre-calibrated with respect to the C 1s core level at 284.8 eV. The atomic concentration ratios were calculated from the integral photoelectron peak intensities (O 1s, Al *2p*, La *3d* and Pt *4d*). The fittings were in a XPSpeak1 software and determined with different proportions of Lorentzian and Gaussian functions.

The dehydrogenation of cyclohexane to benzene was used to estimate the Pt dispersion by an indirect method. As the dehydrogenation of cyclohexane is a structure insensitive reaction, its rate is independent of the dispersion of the metal on the surface, as previously demonstrated [18]. The catalytic runs were performed in a continuous fixed bed quartz reactor at atmospheric pressure using 10 mg of the catalyst powders, which were loaded into the fixed-bed reactor at atmospheric pressure. Before the catalytic activity tests, the catalysts were reduced *in situ* in the reactor using a $H_2$ flow (30 mL $min^{-1}$) at 650 °C for 2 h. The reaction was conducted at 170 °C with a WHSV of 170 $h^{-1}$ by feeding the cyclohexane to the reactor. The gas products were analyzed using a HPINNOWAX capillary column in the HP5890 gas chromatograph.

### 2.3. Catalytic evaluations

#### 2.3.1. Steam reforming of methane (SRM)

The steam reforming of methane tests were carried out in a fixed bed continuous flow quartz reactor possessing an internal diameter of 8 mm. The reaction temperature was monitored by a type K thermocouple placed inside the catalyst bed that allows controlling the reaction temperature. The reactor was charged with 100 mg of the samples. Before the catalytic runs, the samples were previously reduced to 650 °C under a $H_2$ flow at 30 mL $min^{-1}$. For a typical reaction, a $CH_4$:$H_2O$:$N_2$ feed composition possessing a ratio of 1:3:0.4 (total flow rate of 2 × $10^{-2}$ mol $min^{-1}$) was introduced to the reactor at atmospheric pressure. The reaction temperature was varied from 410 to 510 °C to achieve a 13% of conversion. Further details of the activation energy and TOF calculations as well as additional data are found in ref. [24]. The resulting effluent gas products were then analyzed by an on-line gas chromatography using a Varian-340 with a TCD detector. For reaction product analysis, the Porapak N and Molecular Sieve 13X were connected in a series of parallel columns and attached with the TCD for product separation. The reactants and products components e.g, $CH_4$, CO, $CO_2$, $H_2$ and $H_2O$ were detected, but $H_2O$ was not quantified.

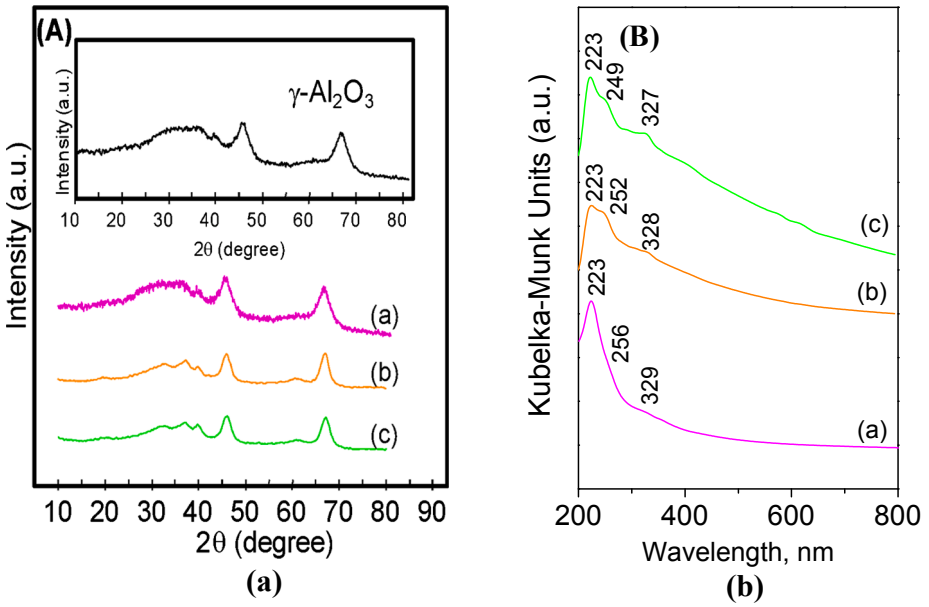


**Fig. 1.** (A) XRD patterns and (B) DRS spectra of the fresh catalysts: (a) Pt (0.5 wt%)/$Al_2O_3$-$La_2O_3$, (b) Pt(1.0 wt%)/$Al_2O_3$-$La_2O_3$ and (c) Pt(2.0 wt%)/$Al_2O_3$-$La_2O_3$. The inset figure is the XRD pattern of the $Al_2O_3$-$La_2O_3$ support.

**Table 1**
The BET surface area ($S_{BET}$), pore volume ($V_p$) and average pore diameter ($D_p$) of the solids studied.

| Catalysts | $S_{BET}$ ($m^2.g^{-1}$) | $V_p$ ($cm^3.g^{-1}$) | $D_p$ (nm) |
|---|---|---|---|
| Pt (0.5 wt%)/$Al_2O_3$-$La_2O_3$ | 119 | 0.17 | 6.4 |
| Pt(1.0 wt%)/$Al_2O_3$-$La_2O_3$ | 89 | 0.16 | 7.2 |
| Pt(2.0 wt%)/$Al_2O_3$-$La_2O_3$ | 105 | 0.15 | 6.5 |

### 2.3.2. Partial oxidation of methane (POM)

Catalytic performances of the solids were investigated in the partial oxidation of methane (POM) using a fixed-bed down flow reactor at atmospheric pressure. About 40 mg of the samples were mixed with the diluent e.g., 72 mg of SiC and then, placed in the quartz tube reactor under nitrogen flow (30 mL $min^{-1}$) for 0.5 h at 150 °C. Subsequently, the samples were reduced using hydrogen flow at 30 mL $min^{-1}$ for 2 h at 650 °C. Next, the reaction mixture consisting of $CH_4$:$O_2$:$N_2$ with a molar ratio of 2:1:0.9 was introduced into the reactor and the total flow of the mixture was 130 mL $min^{-1}$ with a WHSV = 80 $h^{-1}$. The reaction was conducted at 800 °C. The product concentrations were measured online with a gas chromatography (Varian 3800 CX) using a Chrompack CP-Wax 57 CB capillary column coupled to a FID detector Test-201. An exception of $H_2O$, all other reactants and products such as $CH_4$, $O_2$, CO, $CO_2$ and $H_2$ were quantified using the aforesaid Varian 3800 CX instrument.

Methane conversion (% $X_{CH_4}$) and selectivities of $CO_2$, CO and $H_2$, as well as the reaction rates were obtained by their usual definitions:

$$\%\, X_{CH_4} = \frac{FCH_{4\,in} - FCH_{4\,out}}{FCH_{4\,in}} \times 100 \quad (1)$$

$$\%\, S_{CO_2} = \frac{mols\ of\ CO_{2\,out}}{mols\ of\ CO_{2\,out} + mols\ of\ CO_{out}} \times 100 \quad (2)$$

$$\%\, S_{CO} = \frac{mols\ of\ CO_{out}}{mols\ of\ CO_{2\,out} + mols\ of\ CO_{out}} \times 100 \quad (3)$$

$$\%\, S_{H_2} = \frac{mols\ of\ H_{2\,out}}{mols\ of\ H_{2\,out} + mols\ of\ H_2O_{out}} \times 100 \quad (4)$$

$$r_{CH_4} = \frac{FCH_{4\,in} - FCH_{4\,out}}{w_{cat}\ .\ time} \quad (5)$$

where $F_{in}$ and $F_{out}$ represent the flow of the gas fed in the reactor and flow of the gas coming out of the reactor, respectively. Selectivity values were calculated from the abovementioned flow of the products obtained. $w_{cat}$ and time indicate the catalyst weight and the reaction time, respectively.

## 3. Results and discussion

### 3.1. Structural properties through XRD and UV–Visible measurements

Fig. 1A depicts the XRD patterns of the fresh Pt($x$ wt%)/$Al_2O_3$-$La_2O_3$ catalysts. All the peaks are assigned to be from the cubic γ-$Al_2O_3$ (*Fd-3m* space group JCPDS 10-425). Moreover, the variations of the Pt loadings do not affect the crystallinity of the solids. This could be explained based on the fact that a 12 wt% of $La_2O_3$ is successfully incorporated in the γ-$Al_2O_3$ framework, as found elsewhere [18]. Another point is that the good dispersion of Pt on the solid surface may take place, even at high loadings of ca. 2.0 wt%. Thus, it could be assumed that the sizes of the Pt particles for samples having high Pt loadings are not visible in the XRD patterns due to the limitation of the technique.

The diffuse reflectance experiments (DRS) are used to predict the geometric and electronic properties of the Pt on the fresh Pt($x$ wt%)/$Al_2O_3$-$La_2O_3$ catalysts. The charge-transfer bands from the oxygen coming from the support or chloride ions to Pt are represented by a broad band with maximum intensity at 224 nm for Pt(0.5 wt%)/$Al_2O_3$-$La_2O_3$ catalyst (Fig. 1B). Due to the d-d transitions of Pt, a vibrational frequency peak is detected at 333 nm, in agreement with the findings [24–26].

Notably, the relative intensity of the bands decreases significantly while the charge transfer and d-d transitions bands became more visible with increasing the Pt loading onto the supports; consequently, the peaks are shifted to higher frequencies. This indicates a lesser degree of Pt interactions with alumina and lanthana. It may also be assigned to the metal-support interaction between $[Pt^{IV}(OH)_4Cl_2]_s$ or yet, $(PtO_xCl_y)_s$ type species and $Al_2O_3$-$La_2O_3$ support surface [18]. Furthermore, the presence of $PtO_2$ species with big PtO particles may facilitate the increase of the d-d transitions band. In addition, the charge-transfer bands are shifted toward higher energy for Pt(2.0 wt%)/$Al_2O_3$-$La_2O_3$ compared with Pt(1.0 wt%)/$Al_2O_3$-$La_2O_3$ and Pt(0.5 wt%)/$Al_2O_3$-$La_2O_3$ catalysts. This can indicate that a lesser metal-support interaction may somewhat occur in the former solid.

### 3.2. Textural properties and morphological aspects by SEM and TEM

The textural properties of the solids are listed in Table 1. According to our previous work, the $Al_2O_3$-$La_2O_3$ support has BET surface area of 191 $m^2\,g^{-1}$ with pore volume value of ca. 0.17 $cm^3\,g^{-1}$ [18]. The BET surface areas of the Pt($x$ wt%)/$Al_2O_3$-$La_2O_3$ are in the 89–119 $m^2\,g^{-1}$ range with the correspondent pores volumes of 0.15–0.17 $cm^3\,g^{-1}$. The reason for the decrease of the textural properties seems to indicate that the Pt incorporation to the support may promote, in some extent, a blockage of the pore, especially for high amounts of Pt as 2 wt%. Also, Pt dispersion on the support is favored due to the lanthana presence, as found in our previous work [15], even at higher Pt loadings as 2.0 wt%. These observations are in line with XRD measurements.

Additionally, pore diameters values of Pt(0.5 wt%)/$Al_2O_3$-$La_2O_3$ and Pt(2.0 wt%)/$Al_2O_3$-$La_2O_3$ are quite similar whereas the pore diameter of Pt(1.0 wt%)/$Al_2O_3$-$La_2O_3$ is slight higher than the other solids, most probably due to the different sizes of Pt dispersed on the pore mouths of the later samples.

After being reduced, a distribution of the randomly Pt particles on solid surface is seen through the white dots of the SEM image and histogram of Pt(0.5 wt%)/$Al_2O_3$-$La_2O_3$ (Fig. 2a). Besides, $La_2O_3$ is still homogeneously incorporated to alumina support, especially in the close contact with Pt particles (as seen in the EDS spectra of the high magnification SEM image). For Pt(2.0 wt%)/$Al_2O_3$-$La_2O_3$ (Fig. 2b), the surface seems to be rough comparing with the 0.5 wt% counterpart. Also, the Pt particles become larger with the consequent growth upon reduction (as seen in the magnification SEM image). Indeed, the histogram of Pt(0.5 wt%)/$Al_2O_3$-$La_2O_3$ shows that the average particles size is 12 nm. According to the EDS elemental analyses, the platinum particles are supposed to be around the La and Al elements.

Our previous reports show that the TEM images of the fresh samples possessing Pt loadings of 0.5 wt% display the distribution of Pt on solid surface [15,22]. When reduced, the Pt particles sizes of Pt(0.5 wt%)/$Al_2O_3$-$La_2O_3$ catalyst varies from 3 to 15 nm (black dots in the left TEM image, Fig. 2c), which is much bigger than those on the fresh solid. The HRTEM image (included figure in the left image) shows that the lattice fringes found for reduced Pt(0.5 wt%)/$Al_2O_3$-$La_2O_3$ sample is 0.23 nm, which is attributed to be from (1 1 1) plane of metallic Pt. With increasing the Pt loadings to 2.0 wt%, the deposition of bigger Pt particle on the support is observed in the TEM image of the reduced Pt (2.0 wt%)/$Al_2O_3$-$La_2O_3$ sample (Fig. 2c, right side). Moreover, the HRTEM image in the lower right panel demonstrates that a d spacing of 0.19 nm corresponds to the (2 0 0) plane of PtO nanoparticles while the lattice fringe value of 0.23 nm is due to $Pt^o$. Also, these Pt particles are in close contact to each other and have sizes of ca. 5–18 nm; thus, one can assume that these particles suffered from sintering during the reduction for a 2.0 wt% of Pt.

Thus, the results indicate that high Pt loadings in Pt($x$ wt%)/$Al_2O_3$-

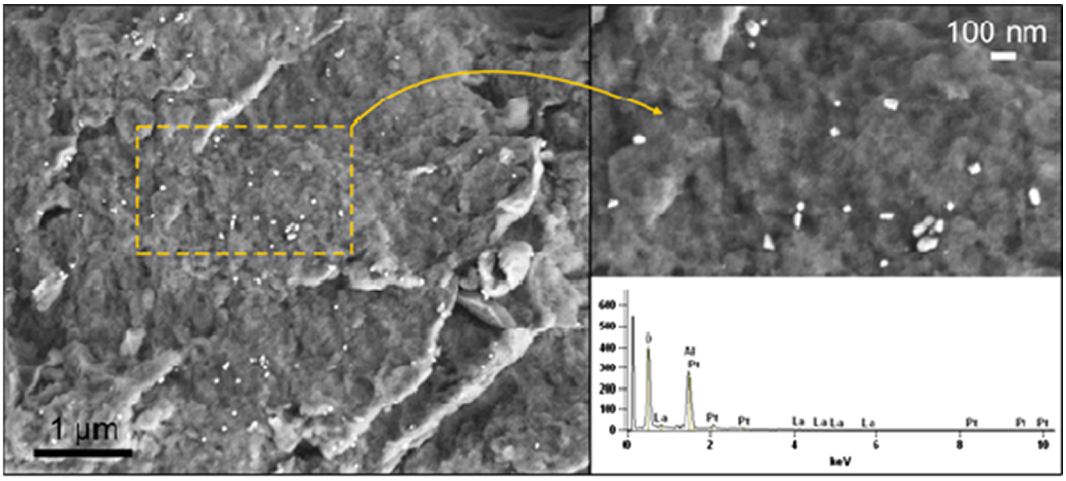


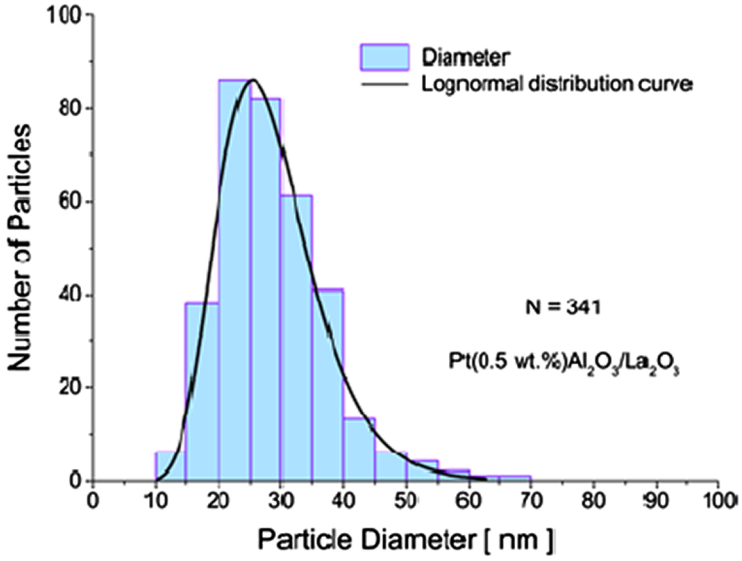


(a)

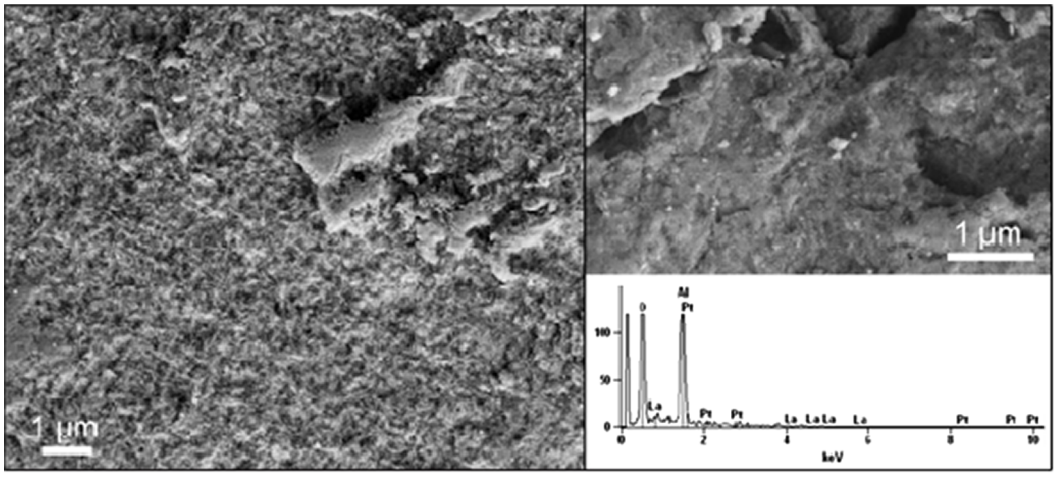


(b)

**Fig. 2.** (a) The SEM images of the reduced Pt(0.5 wt%)/$Al_2O_3$-$La_2O_3$ solid. The included figure is the EDS spectrum of the sample. The panel includes the histogram of particle size distribution of the solid. (b) The SEM images of the reduced Pt(2.0 wt%)/$Al_2O_3$-$La_2O_3$ sample. The included figure is the EDS spectrum of the sample. (c) TEM image of Pt(0.5 wt%)/$Al_2O_3$-$La_2O_3$ is in the left side of the panel. TEM image of Pt(2.0 wt%)/$Al_2O_3$-$La_2O_3$ is in the right side of the panel. The High-resolution TEM images are included.

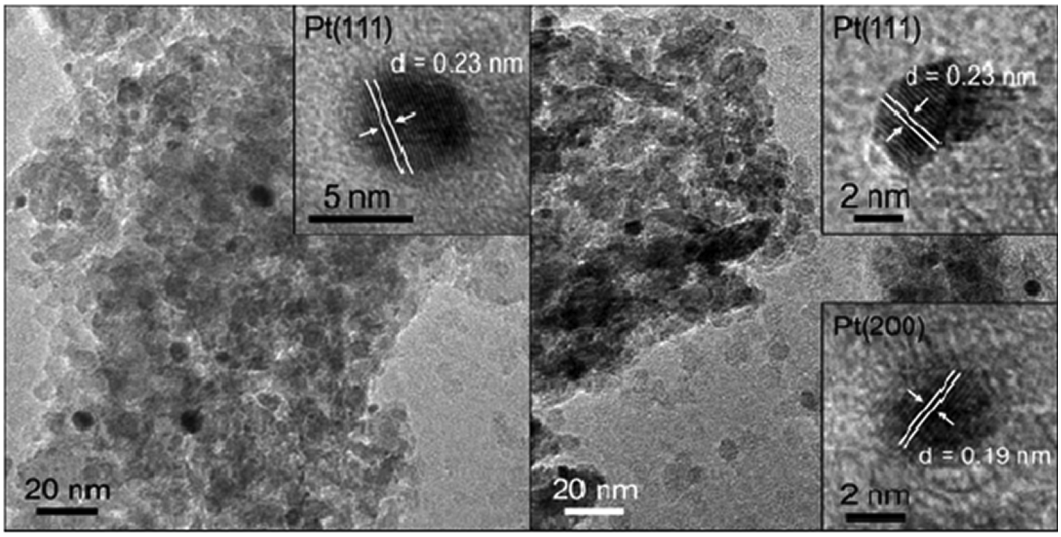


**Fig. 2.** (*continued*)

$La_2O_3$ catalysts can promote the formation of relatively bigger Pt particles on the $Al_2O_3$-$La_2O_3$ surface. Although the addition of lanthana greatly improves the Pt dispersion of the Pt(*x* wt%)/$Al_2O_3$-$La_2O_3$ samples, big Pt particles are formed due to the sintering with increasing Pt loadings.

### 3.3. $H_2$-TPR and CO-DRIFTS analyses

The TPR profiles of the Pt(*x* wt%)/$Al_2O_3$-$La_2O_3$ catalysts are depicted in Fig. 3A.

The profiles of the $Al_2O_3$-$La_2O_3$ support do not display any reduction peaks below 1000 °C [15]. Thus, any observed reduction peaks of the Pt(*x* wt%)/$Al_2O_3$-$La_2O_3$ catalysts are strictly due to the reduction of the platinum oxide species. The TPR profile of the Pt(0.5 wt%)/$Al_2O_3$-$La_2O_3$ catalyst depicts reduction peaks at 220 and 403 °C with a shoulder arising at 523 °C. Accordingly, the first peak is assigned to the reduction of $[Pt^{IV}(OH)_4Cl_2]_s$ species while the second one is attributed to the reduction of the $[Pt^{IV}O_xCl_y]_s$ species [18]. The reduction peaks shift to low temperatures with increasing the Pt loadings. This could indicate an increase of $PtO_x$-$PtO_x$ networks with the support. Literature results suggest that the $PtO_x$ particle sizes, loadings, dispersion and degree of oxidation may affect the TPR profile, as in the case of $PtO_x$ supported on alumina [18 (and references herewith).]. Therefore, it is not possible to determine which parameter is relevant for the shifts of the reduction temperatures.

In line with TEM and UV–Vis results, the size of the Pt particles in the Pt(*x* wt%)/$Al_2O_3$-$La_2O_3$ catalysts slight increased with raising the Pt loadings. As a consequence, an easier reduction of the Pt particles is seen for samples having higher Pt loadings, mostly due to the Pt particles agglomeration. Furthermore, the TPR profiles for samples possessing Pt loading higher than 0.5 wt% exhibit quite similar reduction behavior to that of Pt(0.5 wt%)/$Al_2O_3$-$La_2O_3$, except the more evident

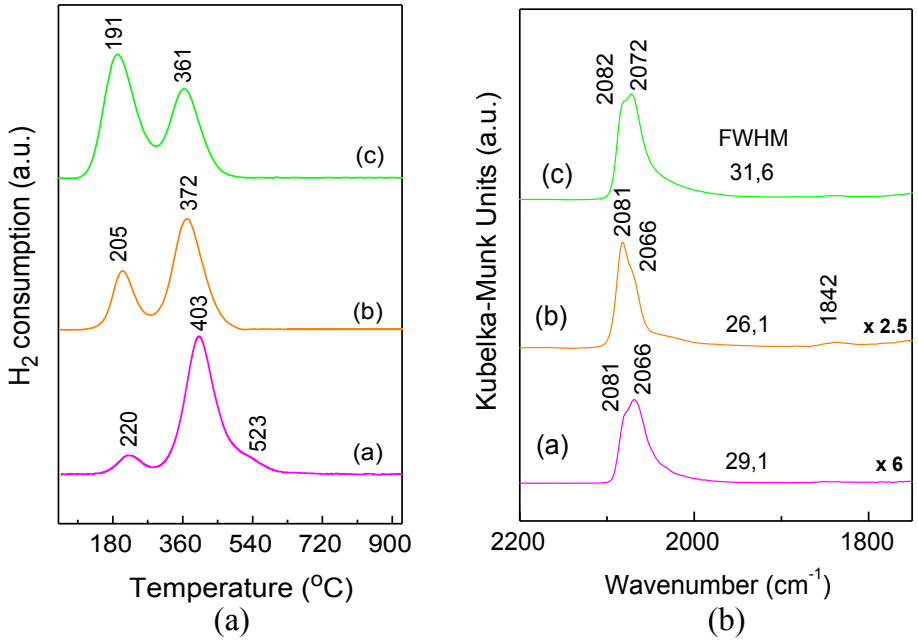


**Fig. 3.** (A) TPR curves of the fresh Pt(*x* wt%)/$Al_2O_3$-$La_2O_3$ catalysts (B) DRIFTS of adsorbed CO spectra of the Pt(*x* wt%)/$Al_2O_3$-$La_2O_3$ reduced catalysts. The samples are labeled as follows: (a) Pt(0.5 wt%)/$Al_2O_3$-$La_2O_3$, (b) Pt(1.0 wt%)/$Al_2O_3$-$La_2O_3$ and (c) Pt(2.0 wt%)/$Al_2O_3$-$La_2O_3$.

shoulder at 523 °C, in reason of non-stoichiometric $La_2O_3$ formation.

The low temperature *in situ* DRIFTS with CO adsorption experiments aim to study the surface properties of the Pt particles and their interactions with CO. The CO-DRIFTS spectra (Fig. 3B) depict a board band with maxima at 2063 $cm^{-1}$, which is assigned to CO adsorption linearly bonded to under-coordinated sites such as step, edge and corners [27]. Another component is a shoulder at 2081 $cm^{-1}$, which is ascribable to CO linearly bound to well-coordinated terrace Pt (1 1 1) facets as well as the $Pt^o$ (CO) species from the higher reducibility of Pt oxide by CO [18,27,28]. Rising the Pt loadings for more than 0.5 wt%, the CO bands shift to high frequencies regions and increased their intensities. Simultaneously, at low frequencies regions, the appearance of a low intensity band at 1842 $cm^{-1}$ suggests that the CO interaction with two surface Pt atoms on bridged Pt entities [18,26], which are geometrically favored on terrace sites [26,28].

These changes to higher frequencies regions with Pt loadings > 0.5 wt% are clearly caused by the CO adsorption in distinct Pt particles sizes. Despite these shifts in the peak positions to higher frequencies, the increase of Pt loadings results in a significant increase of the FWHM, except for Pt(1.0 wt%)/$Al_2O_3$-$La_2O_3$. For instance, the FWHM of the Pt (2.0 wt%)/$Al_2O_3$-$La_2O_3$ is 31.6 whereas that of Pt(0.5 wt%)/$Al_2O_3$-$La_2O_3$ is 29.1. This suggests a broad distribution of Pt particles with different sizes on the former sample and consequently, distinct electronic density on solid surface. Importantly, the CO linearly chemisorbed on negatively charged Pt sites should appear as peaks at around 2020 and 1970 $cm^{-1}$ [28]. This would account for the exposed Pt sites and the strongly basic oxygen anions of the La and hydroxyl Al components. The results of TEM and TPR analysis support these conclusions.

### 3.4. Surface properties local environment of the Pt species by XPS

The oxidation state and surface atomic composition of the fresh oxidized and reduced catalysts are determined via X-ray photoelectron spectroscopy. The binding energies (BE) of the corresponding O 1s, Al *2p*, La $3d_{5/2}$ and Pt $4d_{5/2}$ core electrons are presented in Table 2.

The BE of O *1s* is 531.1 eV for all solids, which confirms the presence of bulk oxygen coming from the support, in accordance with the XRD and DRS measurements. To confirm these results, the Al *2p* core level of the fresh sample is BE of 74.4 eV, being associated with the contributions of the $Al^{3+}$ species [15,29,30]. Indeed, La exists as $La^{3+}$ from $La_2O_3$, according to the La $3d_{5/2}$ BE values of ca. 835.3 eV for the fresh solids. This is in line with the BE values found for lanthana supported-catalysts [18]. In reason of the overlapping of the Al *2p* core level with that of the Pt *4f* one [31], the Pt *4d* core levels are considered in this work. Thereby, XPS analyses for Pt $4d_{5/2}$ core level display BE value of 315.2 eV, implying that $Pt^{2+}$ species exist as PtO [15]. This corroborates with the DRS measurements. Noteworthy, the binding energies presented are close to those found in the reports for $Pt^{2+}$ and $Pt^{4+}$ species, respectively 317.1–317.7 eV and 314.6–314.7 eV [31–34]. One can observe from Table 2 that the surface Pt/La + Al atomic ratios increase with increasing the Pt loadings in all solids. There is now a clear enrichment of Pt species on the Pt(*x* wt%)/$Al_2O_3$-$La_2O_3$ surfaces and this effect is remarkable with rising the Pt loadings, as seen in the solid possessing 2 wt% of Pt.

The reduced catalysts have O 1s core-level of 529.8 eV, being assigned to the lattice oxygen i.e., *Oα*, besides a small contribution of Pt-O-like species at 530 eV [31], as shown by the Pt(0.5 wt%)/$Al_2O_3$-$La_2O_3$ solid. With rising the Pt loadings for more than 0.5 wt%, higher values of BE can be attributed to *Oβ* chemisorbed oxygen of the support [31]. Moreover, BE of Al *2p* core level of the reduced solids is in the 72.9–74.5 eV range, assigning the existence of $Al^{3+}$ species [18]. Also, La $3d_{5/2}$ BE values remain unchanged in comparison with the fresh solids. As expected, the supports are unaffected with the reduction process, although the BE of La $3d_{5/2}$ core level for Pt(0.5 wt%)/$Al_2O_3$-$La_2O_3$ solid is significantly lower e.g. 834.2 eV compared to the others reduced ones. This may indicate a strong La interaction with Pt species and $Al_2O_3$ support in Pt(0.5 wt%)/$Al_2O_3$-$La_2O_3$.

Also, BE of Pt $4d_{5/2}$ core levels changes from 315.2 to 314.0 eV illustrating that the reduction of the species is accompanied by the formation of $Pt^o$ particles (HRTEM results), as found elsewhere [18]. When the Pt loadings increases, a substantial decrease of the BE is noted, as in the case of Pt(2.0 wt%)/$Al_2O_3$-$La_2O_3$. These differences are attributed to the fact that the high Pt loadings gives exposed $Pt^o$ particles leading to low metal–support interaction with γ-$Al_2O_3$. This is possibly due to the contribution of the lanthana surface facilitating the reduction of the Pt entities (TPR and CO-DRIFTS results), likewise to other Pt-supported LaAl catalysts [9,35]. In agreement, the Pt/Al + La noticeably increased with high Pt loadings more than 0.5 wt%, confirming that the Pt species located on the surface of the solids is weakly bounded to the support. Besides, the Pt particles covering by the support is decreased with increasing the Pt particles sizes. These facts are in accordance with the results of TEM and CO-DRIFTS.

### 3.5. Cyclohexane dehydrogenation to benzene

The cyclohexane dehydrogenation to benzene reaction is performed to further evaluate the properties of platinum particles dispersion on the supports. Considering the fact that the reaction is insensitive to structure, the cyclohexane is found to dehydrogenate on Pt sites with rates justifying the extent of the density of available Pt sites for the reaction at certain temperatures [18]. The rates of cyclohexane dehydrogenation are shown in Table 3.

From Table 3, the $r_d$ of Pt(0.5 wt%)/$Al_2O_3$-$La_2O_3$ is $2.25 \times 10^{-5}$ mol $s^{-1}$ g $cat^{-1}$ with the corresponding 34% of Pt dispersion. It has been well documented that the cyclohexane is chemisorbed over the Pt sites with the consequent hydrocarbon dehydrogenation. The reaction takes place over well dispersed Pt particles e.g., $Pt^o$ or $Pt^{2+}$ on the $Al_2O_3$-$La_2O_3$ support surface [18,36,37].

Moreover, the rate of cyclohexane dehydrogenation increases from $2.25 \times 10^{-5}$ to $7.60 \times 10^{-5}$ mol $s^{-1}$ g $cat^{-1}$, respectively with loadings of 0.5 and 2.0 wt%. The relative amount of Pt dispersed on the Pt(*x* wt%)/$Al_2O_3$-$La_2O_3$ catalyst is of ca. 34–36%. The findings states that the degree of cyclohexane coordination to Pt atoms is the driving force for the elimination of a hydride molecule and form benzene on solid surface [36]. Thereby, the Pt dispersion determines the observed rates of the reaction.

### 3.6. Catalytic results

#### 3.6.1. Steam reforming of methane (SRM)

The Arrhenius plot illustrates the effects of reaction temperature on the catalytic performances of the solids (Fig. 4).

Plots clearly demonstrate that the apparent activation energy is 70 kJ $mol^{-1}$ for all Pt(*x* wt%)/$Al_2O_3$-$La_2O_3$ catalysts (Table 3), independently of the Pt loadings.

**Table 2**
Bindings energies (BE) and surface atomic ratios obtained from XPS spectra of the oxidized and reduced catalysts.

| Catalysts | | BE (eV) | | | | Pt/Al + La |
|---|---|---|---|---|---|---|
| | | O 1*s* | Al 2*p* | La $3d_{5/2}$ | Pt $4d_{5/2}$ | |
| Pt(0.5 wt.%)/$Al_2O_3$-$La_2O_3$ | Oxid.[a] | 531.3 | 74.4 | 835.3 | 315.2 | 0.0042 |
| | Red[b]. | 529.8 | 72.9 | 834.2 | 314.0 | 0.0040 |
| Pt(1.0 wt.%)/$Al_2O_3$-$La_2O_3$ | Oxid.[a] | 531.4 | 74.5 | 835.5 | 315.1 | 0.0099 |
| | Red.[b] | 532.2 | 74.5 | 835.5 | 313.9 | 0.0084 |
| Pt(2.0 wt.%)/$Al_2O_3$-$La_2O_3$ | Oxid.[a] | 531.1 | 74.6 | 835.7 | 315.2 | 0.0235 |
| | Red.[b] | 531.0 | 74.5 | 835.6 | 313.6 | 0.0205 |

[a] Fresh samples oxidized in air at 350 °C.
[b] Samples reduced at 650 °C.

**Table 3**
The dispersion of Pt ($D_{Pt}$), rates of cyclohexane dehydrogenation ($r_d$), conversion of methane ($X$) and steam reforming of methane ($r_{SRM}$) reactions of the solids studied. The activation energies ($E_{app}$) and turnover frequency ($TOF$) for SRM and POM are also shown.

| Catalysts | Cyclohexane dehydrogenation[a] | | SRM[b] | | | POM[c] | | |
|---|---|---|---|---|---|---|---|---|
| | $D_{pt}$ (%) | $r_d 10^{-5}$ (mol $s^{-1}$ $gcat^{-1}$) | $E_{app}$ (kJ.$mol^{-1}$) | $r_{SRM} 10^{-1}$ (mol $s^{-1}$ $gcat^{-1}$) | $TOF$ ($s^{-1}$) | $r_d/r_{srm}$ | $TOF$ ($s^{-1}$) | %X[d] |
| Pt (0.5 wt%)/$Al_2O_3$-$La_2O_3$ | 34 | 2.25 | 70.3 | 7.26 | 11.8 | 0.3 | 105.7 | 78 |
| Pt(1.0 wt%)/$Al_2O_3$-$La_2O_3$ | 36 | 4.03 | 70.6 | 5.91 | 3.1 | 0.7 | 46.2 | 76 |
| Pt(2.0 wt%)/$Al_2O_3$-$La_2O_3$ | – | 7.60 | 70.8 | 4.58 | – | 1.6 | – | 74 |

[a] Rate of cyclohexane dehydrogenation at 270 °C.
[b] Rate and TOF for steam reforming methane at 500 °C [18].
[c] TOF for partial oxidation of methane at 800 °C and 0.5 h.
[d] X is the methane conversion for POM in 0.5 h of reaction.

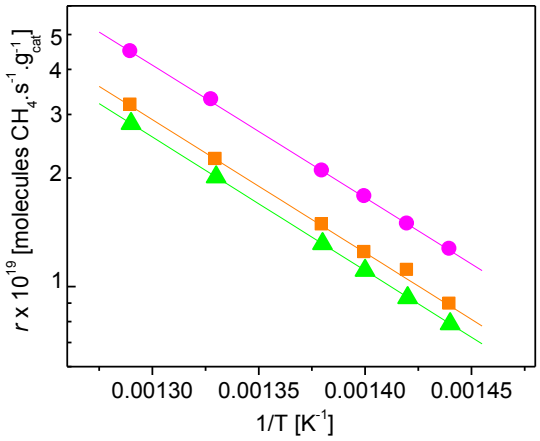


**Fig. 4.** Arrhenius plots for steam reforming of $CH_4$ over Pt($x$ wt%)/$Al_2O_3$-$La_2O_3$ catalysts with different Pt loading: 0.5 wt% (●), 1.0 wt% (■), and 2.0 wt% (▲).

Overall, the Pt($x$ wt%)/$Al_2O_3$-$La_2O_3$ catalysts depict similar values of $E_{app}$, but the catalytic activity of the solids varies in the SRM, depending on the Pt loadings. Thus, the data in Table 3 demonstrate that the surface Pt sites increases with raising the Pt loadings (cyclohexane dehydrogenation rates data and CO-DRIFTS results). Based on above evidences, it can be speculated that the $CH_4$ and $H_2O$ environments give the PtO and $Pt^o$ species formation. Thereby, under SRM conditions, the chlorined $PtO_x$ species are partially oxidized to PtO in the presence of steam; consequently, the catalyst begins to be transformed into $Pt^o$, when $CH_4$ is introduced in the media. Although there is considerably more platinum in the Pt(2.0 wt%)/$Al_2O_3$-$La_2O_3$ catalyst than the 1.0 wt % counterparts, the $E_{app}$ values are obviously very similar indicating the existence of $Pt^o$ and PtO entities. Moreover, the $E_{app}$ values give results comparable to those of Pt and Pd dispersed on $CeO_2$–$Al_2O_3$ catalysts for SRM [38,39].

Specific reaction rate, expressed as $r_{SRM}$ is 7.26 mol $s^{-1}$ $gcat^{-1}$ and the corresponding TOF was 11.8 $s^{-1}$ for the Pt (0.5 wt%)/$Al_2O_3$-$La_2O_3$ catalyst. Both $r_{SRM}$ and TOF values followed a trend of decrease for Pt loadings higher than 0.5 wt%. This is consistent with the sintering effects, as latter shown. Moreover, the $r_{SRM}$ and TOF values (Table 1) indicate that the activity of the catalysts in the SRM reactions is decreased due to the carbonaceous species formation. This demonstrates the superiority of Pt(0.5 wt%)/$Al_2O_3$-$La_2O_3$ in SRM over the other solids possessing higher Pt loadings. Regarding the metal-support interactions, the Pt nanoparticles dispersed on the support having a strong interaction greatly improve the Pt particles stability against sintering, as in the case of Pt(0.5 wt%)/$Al_2O_3$-$La_2O_3$ catalyst.

Also, the ratio between cyclohexane dehydrogenation and steam reforming ($r_d/r_{SRM}$) is of ca. 0.3 for Pt(0.5 wt%)/$Al_2O_3$-$La_2O_3$ catalyst and the $r_d/r_{SRM}$ ratios rise with increasing the Pt loadings for more than 0.5 wt%. The discrepancy in the catalytic behavior of the solids in the cyclohexane dehydrogenation and SRM is because of the lanthanum may be in close contact with small Pt particles dispersed on the support, at particular loadings as 0.5 wt% during the SRM. According to the observations of Araujo *et al.* [18], there is a preferential cyclohexane chemisorption on active Pt sites, but the hydrocarbon accessibility to the $Pt^o$ sites is hindered as an effect of partial coverage of Pt particles by $LaO_x$-Pt specie at low Pt loadings in the cyclohexane dehydrogenation reaction.

As Pt loadings increases, the rates increase due to the Pt participation, albeit the agglomeration of Pt (TEM, TPR and CO-DRIFTS results) inhibits the $LaO_x$-Pt species formation.

### 3.6.2. Partial oxidation of methane (POM)

The effects of Pt loadings on Pt($x$ wt%)/$Al_2O_3$-$La_2O_3$ catalysts are illustrated in the partial oxidation of methane, as shown in Fig. 5. Also, methane conversions values for 0.5 h of time on stream are shown in Table 3.

At the beginning of the reaction, the solids have conversions in the 74–78% range (Fig. 5a, Table 3). The methane conversions experience a decay within the first 7 h of time on stream in all cases, and the catalyst with the highest Pt loading has poor catalytic performance (Fig. 5a). To better appreciate this evidence, $CH_4$ conversion of Pt(0.5 wt%)/$Al_2O_3$-$La_2O_3$ catalyst is superior to 79% while Pt(2.0 wt%)/$Al_2O_3$-$La_2O_3$ one has its performance below to this value due to heavy carbonaceous deposition and sintering of the Pt particles (latter shown by XPS, SEM and TEM of the spent solids). Following the idea that the incorporation platinum species into the support would permit homogeneous distribution of the Pt on solid surfaces, the resultant catalytic performance of the Pt(2.0 wt%)/$Al_2O_3$-$La_2O_3$ is found to be significantly affected by the amount of exposed Pt sites (Table 3). Images from SEM and TEM microscopy, CO-DRIFTS and TPR measurements demonstrate that the reduction leaves behind 5–35 nm sized Pt particles in the Pt(2.0 wt %)/$Al_2O_3$-$La_2O_3$ sample, as seen by the histogram in Fig. 2a. This can be related to the sintering causing the low performance of the solid.

On the contrary, the evolution of the $CH_4$ conversions for samples having lesser than 2.0 wt% of Pt illustrates a very high stability, after 7 h on stream. Most probably, the significant lanthana promoting effects in stabilizing the Pt(0.5 wt%)/$Al_2O_3$-$La_2O_3$ and Pt(1.0 wt %)/$Al_2O_3$-$La_2O_3$ solid should be taking into account, when considering the performance of bare Pt/$Al_2O_3$ analogous in POM reaction [18]. Thus, the solid with a 2.0 wt% of Pt exhibits a very low stability and an evident deactivation, undergoing a very fast $CH_4$ conversion decay after just a few hours because of coking and sintering of the particles effects. The spent sample characterization results will be presented and discussed later to confirm these hypotheses.

The Pt(0.5 wt%)/$Al_2O_3$-$La_2O_3$ catalyst has the best performance along of 24 h of time on stream, among the solids studied. The textural properties in Table 1 demonstrates that the Pt(0.5 wt%)/$Al_2O_3$-$La_2O_3$ catalyst has the major values of textural properties. This could be directly related with the good performance in POM. In accordance with

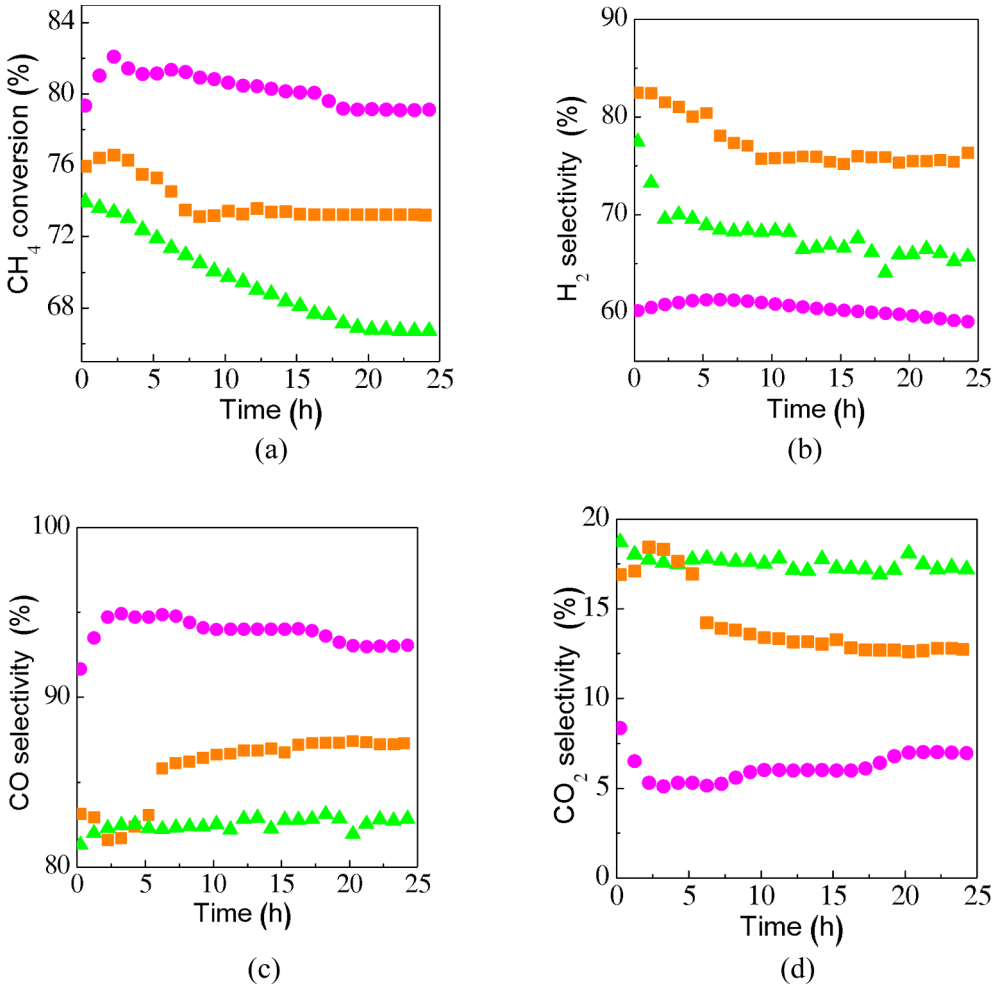


**Fig. 5.** Catalytic evaluation of the solids in the partial oxidation of $CH_4$ reaction at 800 °C for 24 h. (a) The methane conversion and (b) Hydrogen selectivity, (c) Selectivities to $CO_2$ and (d) CO in function of the time on stream for the following samples: (●) Pt(0.5 wt%)/$Al_2O_3$-$La_2O_3$, (■) Pt (1.0 wt%)/$Al_2O_3$-$La_2O_3$ and (▲) Pt(2.0 wt %)/$Al_2O_3$-$La_2O_3$ catalysts in function of time on stream for the following samples:

these results, the number of active sites observed through the TOF for Pt (0.5 wt%)/$Al_2O_3$-$La_2O_3$ is found to be 105.7 $s^{-1}$ whereas the calculated turnover frequency by the Pt(1.0 wt%)/$Al_2O_3$-$La_2O_3$ catalyst is 46.6 $s^{-1}$ with the consequent negligible values of TOF for Pt(2.0 wt%)/$Al_2O_3$-$La_2O_3$ analogue.

Comparing the Pt loadings on Pt(*x* wt%)/$Al_2O_3$-$La_2O_3$ catalysts, it can be inferred that a significantly higher fraction of large Pt particle on Pt(2.0 wt%)/$Al_2O_3$-$La_2O_3$ is not exposed to the reactants due to the big Pt clusters formation and heavy carbonaceous deposits on solid surface (further observed by XPS and TEM of the spent samples), all of these factors accounting for the poorest catalytic performance of the solid.

Overall, the hydrogen selectivities behaviors of the Pt(*x* wt %)/$Al_2O_3$-$La_2O_3$ catalysts have dissimilar trends of those of $CH_4$ conversions (Fig. 5b), which usually do not correspond to only one kind of catalyst in POM reaction. This is especially evident in the case of Pt (1.0 wt%)/$Al_2O_3$-$La_2O_3$ having the highest $H_2$ selectivity of ca. 85% (Fig. 5b) amongst the other solids studied in opposite to its 70% of $CH_4$ conversion in 24 h of time on stream. Next, the selectivity to hydrogen with Pt(0.5 wt%)/$Al_2O_3$-$La_2O_3$ is of ca. 60%, yielding methane conversion of ca. 80%. These results demonstrate that the carbon dioxide can compete with hydrogen to form carbon monoxide and water by reverse gas shift reaction (RGWS) over Pt(0.5 wt%)/$Al_2O_3$-$La_2O_3$, instead of POM occurrence. As shown in Fig. 5b, the Pt(2.0 wt%)/$Al_2O_3$-$La_2O_3$ catalyst exhibits a decline in the $H_2$ selectivity in the 5 h of exposure time, possibly resulted from the easily accumulation of coke deposit on the surface and then, the solid shows an almost constant $H_2$ production but, lower than that of the 1.0 wt% counterpart.

Furthermore, CO selectivities of the Pt(*x* wt%)/$Al_2O_3$-$La_2O_3$ achieve high values (Fig. 5c), when Pt loadings as low as 0.5 wt% are used. This indicates that the reverse water gas shift reaction (RGWS) and dry and steam reforming reactions may take place, with consequent decrease of the hydrogen selectivity for Pt(0.5 wt%)/$Al_2O_3$-$La_2O_3$, as shown in Fig. 5d.

At high Pt loadings, the present Pt(*x* wt%)/$Al_2O_3$-$La_2O_3$ catalysts shows $CO_2$ selectivities values superior to 14% (Fig. 5c), being the Pt (0.5 wt%)/$Al_2O_3$-$La_2O_3$ an exception with a $CO_2$ production nearly to 5% (Fig. 5d). This might be associated with the elevated CO production and its successive disproportion to $CO_2$ and carbon for Pt loadings superior to 0.5 wt% (Fig. 6b). Moreover, the total combustion of methane reaction cannot be ruled out, instead of POM occurrence over Pt loadings higher than 1.0 wt%.

Hence, distinct Pt loadings seems to influence in the POM reaction activity levels with solids deactivation solely observed for higher Pt loadings, in longer periods of reaction. Moreover, the high Pt dispersions and its consequent active sites exposition to $CH_4$ may explain the excellent performance of Pt(0.5 wt%)/$Al_2O_3$-$La_2O_3$ in POM. This behavior of this solid differs from that of the catalyst possessing a 2.0 wt% of Pt loading counterpart that had a declining conversion at the end of the test. It is reasonable to assume that the active Pt species dispersion with La promoter help maintaining the catalyst activity in a stable value all throughout the 24 h of time on stream. Furthermore, Pt(0.5 wt %)/$Al_2O_3$-$La_2O_3$ catalyst shows a good performance in POM, comparing with other catalysts described in the literature, using similar operation conditions [6,7].

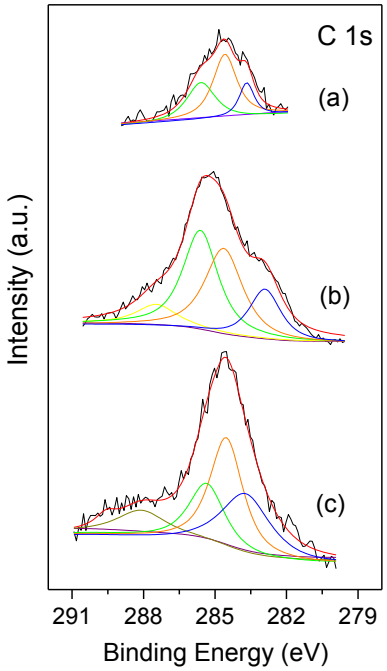


**Fig. 6.** XPS C 1s core-level spectra of catalysts used during 24 h on POM reaction: (a) Pt(0.5 wt%)/$Al_2O_3$-$La_2O_3$, (b) Pt(1.0 wt%)/$Al_2O_3$-$La_2O_3$ and (c) Pt (2.0 wt%)/ $Al_2O_3$-$La_2O_3$.

### 3.7. Characterizations of the spent solids

#### 3.7.1. XPS analyses

As the presence of coke on the catalyst surfaces and sintering of the particles are anticipated to enhance the catalyst's deactivation, the XPS analyses are provided to investigate these phenomena through the surface compositions the solids.

The XPS results reveal the presence of carbon in all spent solids after 24 h of time on stream during POM. It should be noted that the C 1s core levels exhibit five deconvoluted peaks (Fig. 6) with BE at 283.7, 284.6, and 285.7 eV, in the case Pt(0.5 wt%)/$Al_2O_3$-$La_2O_3$ (Table 4).

According to the findings, the peak at around 283.7 eV in the C 1s region is attributed to charge effects whereas the 284.6 eV one is due to the C–C or C–H bonds [40–44]. Also, these results could confirm that the carbon deposition on the solid as $sp^2$ graphitic carbon species such as C═C/C − C in aromatic ring arises at around 283.9–284.4 eV. This corroborates with previous reports on methane transformation reactions [40–42]. Furthermore, the presence of adventitious carbon coming from $CO_2$ and ambient hydrocarbons at around 284.8 eV cannot be ruled out. The BE at around 285.7 eV can be assigned to the C-O or defects [43]. In the meantime, trace amounts of carbonylic/carboxylic species possessing C═O/O–C–O or –C═O bonds from polycarbonates, carbonates and carbon oxygenates are seen with BE of above to 287 eV [42].

Four C 1s peaks are observed for Pt(1.0 wt%)/$Al_2O_3$-$La_2O_3$ assigning from the presence of different kinds of carbon species (Fig. 6). The BE values depicted at around 283.2, 284.5 and 285.6 eV still remain together with a new peak appearing at 287.5 eV. The component at 287.5 eV is related to carbonyl (C═O) and carboxyl groups (COOH or HO–C═O) [41,43]. The similar results can be observed from the BE values at around 283.5 eV assigning the existence of several carbon species e.g., coke-like carbon or chemisorbed $CH_n$ species during methane decomposition [45,46]. Such effects are apparent for Pt(2.0 wt %)/$Al_2O_3$-$La_2O_3$ catalyst (Fig. 6), which has similar BE as those of the parent 1.0 wt% spent solid.

As discussed earlier, this may point to a significantly different surface coke formation amount and its nature, as well. Compositions of the graphitic carbon e.g., 283.9–284.4 eV seem to be high on samples possessing more than 1.0 wt% of Pt. In particular, the peak at 284.4 eV can be assigned $sp^2$ hybridization from filaments of carbon or carbon nanotubes and this value is close to that of the BE at 285.2 eV corresponding to $C_xH_y$ species from methane decomposition [41,42,45].

Thereby, the carbides and graphite carbon growths are significantly enhanced over samples having high Pt loadings at which the reaction rate is below to $9.05 \times 10^{-4}$ mol $s^{-1}$ g $cat^{-1}$ (Table 3). This is due to the contribution of the heavy coke covering the solid surface. On the contrary, even if coke formation is likely over Pt(0.5 wt%)/$Al_2O_3$-$La_2O_3$, the mixture of $CH_4$ and $O_2$ may vanish the coke-like carbon, which is readily oxidized to $CO_2$; consequently, the solid could maintain the best catalytic performance for POM (Table 3) most probably in reason of the strong interaction between Pt nanoparticles and the support.

The XPS surface atomic C/Al ratios are investigated over Pt(*x* wt %)/$Al_2O_3$-$La_2O_3$ spent samples. The C/Al for Pt(0.5 wt%)/$Al_2O_3$-$La_2O_3$ is of ca. 0.11 with the same parameter is of ca.0.70 for Pt(2.0 wt %)/$Al_2O_3$-$La_2O_3$. Indeed, the C/Al + La ratios rise from 0.07 to 0.41, upon increasing the Pt loadings of 0.5–2.0 wt%. This clearly suggests that the conversion of $CH_4$ occurs via POM with the concomitant parallel reactions. Also, it implies that the $CH_4$ is converted into CO, which is further decomposed into coke; methane can be also transformed directly into carbonaceous deposits. More importantly, this is evident as the Pt loadings increase more than 0.5 wt% and corroborates with the fact that the synergetic effect of lanthana and low Pt loadings greatly enhance the catalytic performance through heavy coking alleviation. This is confirmed by the high conversion of 76% for Pt(0.5 wt%)/$Al_2O_3$-$La_2O_3$ (Table 4).

#### 3.7.2. SEM-EDS and TEM

SEM-EDS of the spent solids are shown in Fig. 7.

The carbonaceous deposits are formed in all spent catalysts, after 24 h on stream in POM. The SEM image of Pt(0.5 wt%)/$Al_2O_3$-$La_2O_3$ (Fig. 7a) indicates that the surface comprises exclusively of amorphous carbon (seen in more detail in the top included Fig. 7a). Also, the Pt particles remain exposed on solid surface (EDS spectrum in the top included Fig. 7a). This illustrates that even coking is formed, the Pt nanoparticles are accessible to the reactants and thus, the solid displays a good catalytic performance. Furthermore, the strong metal support interaction enables the complete heavy coking tolerance, which could effectively avoid the catalyst deactivation, as the amorphous carbons are easy to burn with the own the oxygen from the reaction. Accordingly, among the types of deactivating carbon formed during the

**Table 4**
Reaction rates ($r_{CH4}$) taken in 24 h on stream during POM. The surface C/Al and C/La + Al ratios obtained from XPS for the spent catalysts in 24 h of POM.

| Catalyst | $r_{CH4} \times 10^{-4}$ (mol $s^{-1}$ $gcat^{-1}$) | [a]C/Al | [b]C/Al + La | C 1s |
|---|---|---|---|---|
| Pt(0.5 wt%)/$Al_2O_3$-$La_2O_3$ | 9.05 | 0.11 | 0.07 | 283.7<br>284.6<br>285.7 |
| Pt(1.0 wt%)/$Al_2O_3$-$La_2O_3$ | 8.34 | 0.67 | 0.37 | 283.2<br>284.5<br>285.6<br>287.5 |
| Pt(2.0 wt%)/$Al_2O_3$-$La_2O_3$ | 7.59 | 0.70 | 0.41 | 283.7<br>284.5<br>285.3<br>288.0 |

[a] Surface C/Al ratio was determined by ratio between the XPS peaks intensity of C 1s and Al *2p*.

[b] Surface C/Al + La ratio was determined by ratio between the XPS peaks intensity of C 1s and Al *2p* plus La $3d_{5/2}$.

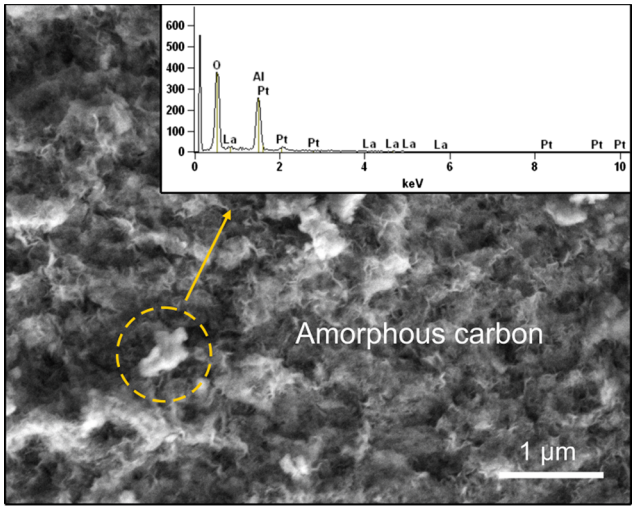


(a)

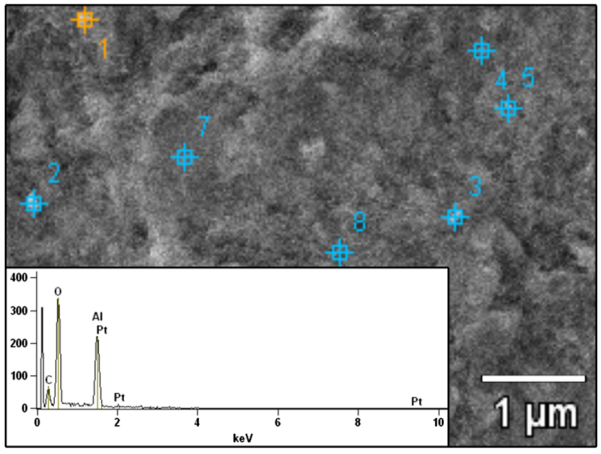


(b)

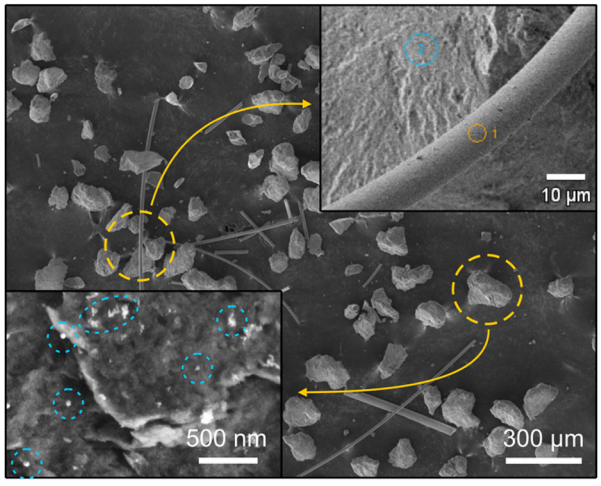


(c)

**Fig. 7.** SEM-EDS images of the spent solids tested in POM reaction, (a) Pt(0.5 wt %)/$Al_2O_3$-$La_2O_3$, (b) Pt(1.0 wt%)/$Al_2O_3$-$La_2O_3$ and (c) Pt(2.0 wt%)/$Al_2O_3$-$La_2O_3$.

reforming reactions, i.e., amorphous, whisker and graphite carbon, the later type is vastly documented to depress the catalyst activity [47], but it is not found over Pt(0.5 wt%)/$Al_2O_3$-$La_2O_3$.

In the case of Pt(1.0 wt%)/$Al_2O_3$-$La_2O_3$, the carbon species are spread over all surface as demonstrated by the numbers in the regions of Fig. 7b. Indeed, the EDS spectrum (in the bottom of Fig. 7b, inset) suggest that La is not visible on the surface indicating that lantana is covered by both amorphous and graphitic carbon species, causing the solid deactivation in some extent. As aforesaid, the graphitic carbon species are well recognized as the major factor that would deactivate the catalyst during POM. For Pt(2.0 wt%)/$Al_2O_3$-$La_2O_3$, the amorphous carbon and whisker carbon filaments formation deposited on the solid surface may effectively cause the catalyst deactivation (seen in the top of Fig. 7c, inset). Also, the circles in the top high magnification included Fig. 7c suggest that the active Pt particles sintering is closely related to the low performance of the catalyst.

TEM is a convenient approach to determine the particle sizes and morphology of the catalysts after the reaction. TEM images of selected spent samples are depicted in Fig. 8.

After testing the solids in 24 h of POM reaction, the Pt particles have a growth with their sizes varying between 1 and 9 nm, as shown by the histogram of the Pt(0.5 wt%)/$Al_2O_3$-$La_2O_3$ solid (Fig. 8a). Moreover, the included high resolution TEM images (Fig. 8a, left) indicate a *d* spacing of 0.23 nm, as indicated by the arrows. This can be attributed to the (1 1 1) face of $Pt^o$, in accordance with XPS results. Also, the HRTEM image (Fig. 8a, right) depicts the Pt (2 0 0) lattice fringes distances of 0.19 nm from PtO, which arises from the reoxidation of $Pt^o$ by oxygen and this agrees with the findings [48,49].

In the case of Pt(2.0 wt%)/$Al_2O_3$-$La_2O_3$, the Pt particles have similar sizes than those of the 0.5 wt% counterpart (histogram of the Fig. 8b). Besides, the $Pt^o$ and PtO particles are highlighted in the top of the included Fig. 8b. This is consistent with the XPS results. Also, the formation of carbon deposits adjacent to the Pt particle are identified as graphitic carbon (0 0 2) plane for Pt(2.0 wt%)/$Al_2O_3$-$La_2O_3$ but, does not depicted in Pt(0.5 wt%)/$Al_2O_3$-$La_2O_3$. Indeed, the HRTEM image reveals the presence of encapsulating carbon deposits coming from the POM reaction for Pt(2.0 wt%)/$Al_2O_3$-$La_2O_3$ (seen in the blue square Fig. 8b HRTEM image). Interestingly, the image HRTEM also illustrates that the Pt particles are in intimately contact with the carbon species.

This is in consistence with our catalytic tests that show a low performance for Pt(2.0 wt%)/$Al_2O_3$-$La_2O_3$ (Fig. 5). In addition, these results agree with the C/Al and the C/Al + La ratios obtained by XPS (Table 3), which suggest the heavy coking on the sample. The findings state that whisker carbon and carbon filaments may decrease the catalysts performance in methane transformations [41]. In addition, Pt is usually the active element that is expected to sinter during the methane conversions [40,41]. In accordance, TEM images of Pt(2.0 wt%)/$Al_2O_3$-$La_2O_3$ also reveals the zones of heterogeneous Pt distribution and coking mainly of amorphous carbon around Pt particles, but this is not observed for Pt(0.5 wt%)/$Al_2O_3$-$La_2O_3$ catalyst.

Based on the observations of Flesh and co-works on Pd/$La_2O_3$ [50], there is a cleaning mechanism of the metal surfaces with the participation of lanthana. Thus, it could represent a catalyst surface reconstruction during POM reaction, which ensures a stronger interaction between Pt particles and the support in the case of Pt(0.5 wt%)/$Al_2O_3$-$La_2O_3$ due to the aforesaid cleaning of the Pt surface; hence, the sample has a lesser heavy carbon deposition, comparable with the Pt loading of 2.0 wt%.

Earlier studies have proposed that $La_2O_3$ presence inhibit Pt sintering due to the anchoring of Pt particles and thus, avoiding the catalyst deactivation [15]. Therefore, a possible mechanism for Pt-containing lanthana catalysts in POM is that the adsorbed $C^*$ formation on

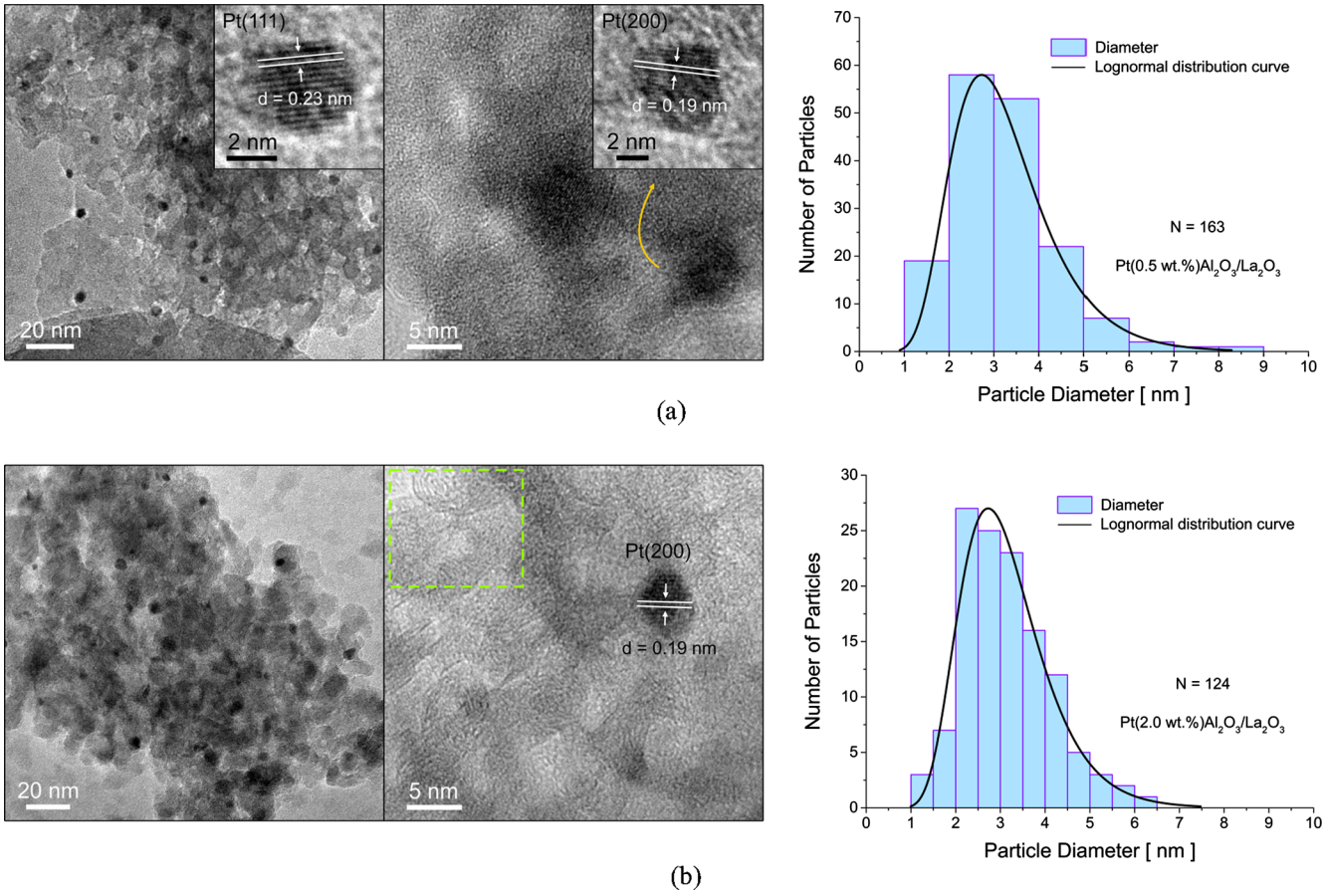


**Fig. 8.** TEM images and histograms of particle diameter distributions for selected spent Pt($x$ wt%)/$Al_2O_3$-$La_2O_3$ catalysts used in the partial oxidation of methane at 800 °C for 24 h: (a) Pt(0.5 wt%)/$Al_2O_3$-$La_2O_3$ and (b) Pt(2.0 wt%)/$Al_2O_3$-$La_2O_3$. The HRTEM images are included.

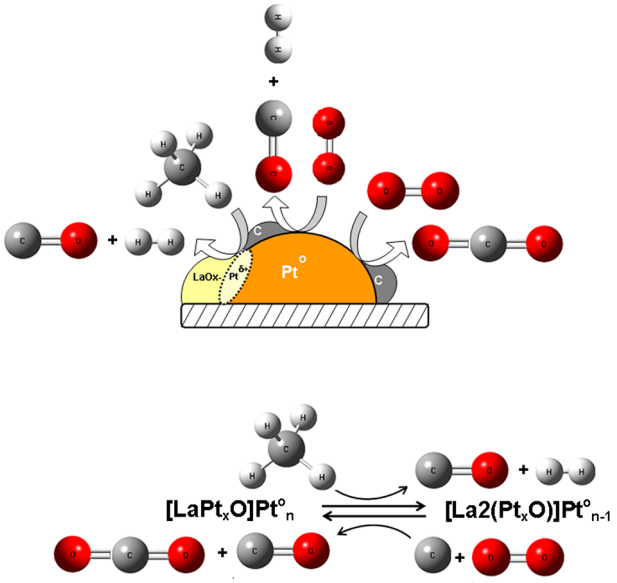


**Fig. 9.** Proposed mechanism for coke C* formed and its subsequent removal on the Pt particles of Pt($x$ wt%)/$Al_2O_3$-$La_2O_3$.

Pt surface is probably a general phenomenon. Then, the following step is a metal complex formation with the participation of lanthana and Pt, namely $[LaPt_xO]Pt^0$ (Fig. 9). This results in the production of CO, $CO_2$ and $H_2$. Simultaneously, the reduced $[La_2Pt_xO]Pt^0_{n-1}$ is generated through the O* transfer to the previous adsorbed C* on Pt surface.

Also, the density functional theory (DFT) studies on the corner, edge and terrace sites of Pt clusters suggest that the $CH_4$ oxidation occurs via C–H bond dissociation over Pt atom site pairs (*–*), in which one of the Pt sites undergoes an oxidative insertion step into the C–H bond [51] and this may confirm the abovementioned observations. Through this mechanistic route, the coke is gasified and the Pt sites become more accessible to $CH_4$, which explains the outstanding conversion of Pt (0.5 wt%)/$Al_2O_3$-$La_2O_3$ compared with the higher Pt loadings counterparts.

### 3.7.3. Raman spectroscopy

The Raman spectroscopy measurements are obtained to a better comprehension of the nature of the coke on the surface of the spent solids. Particularly, the measurements aim to investigate the carbon deposits amorphization or graphitization degree, which may cause the catalyst deactivation phenomena.

The Raman spectra suggest the carbonaceous deposits over all solids, similarly to that other findings in reforming of methane reactions [15,22]. As seen in Fig. 10, the Raman measurements for the spent Pt($x$ wt%)/$Al_2O_3$-$La_2O_3$ catalysts depict two bands at high frequencies regions, after 24 h of POM. In line with earlier reports, the first vibrational mode at around 1345 $cm^{-1}$ is the so called D-band, which is assigned to disordered $sp^2$ hybridized graphite carbon [52,53]. The second one is at 1595 $cm^{-1}$ e.g., the G-band arising from the in-plane bond stretching motion of $sp^2$-hybridized carbon atoms with $E_{2g}$ symmetry in an ideal graphitic lattice [3,52,53,54]. Although lanthana present in all catalysts has a basic character, the Lewis acid sites from γ-$Al_2O_3$ support contribute to the cleavage of methane C–H bond to form coke on the solidssurfaces.

The Pt(2.0 wt%)/$Al_2O_3$-$La_2O_3$ catalyst depicts a major intensity for

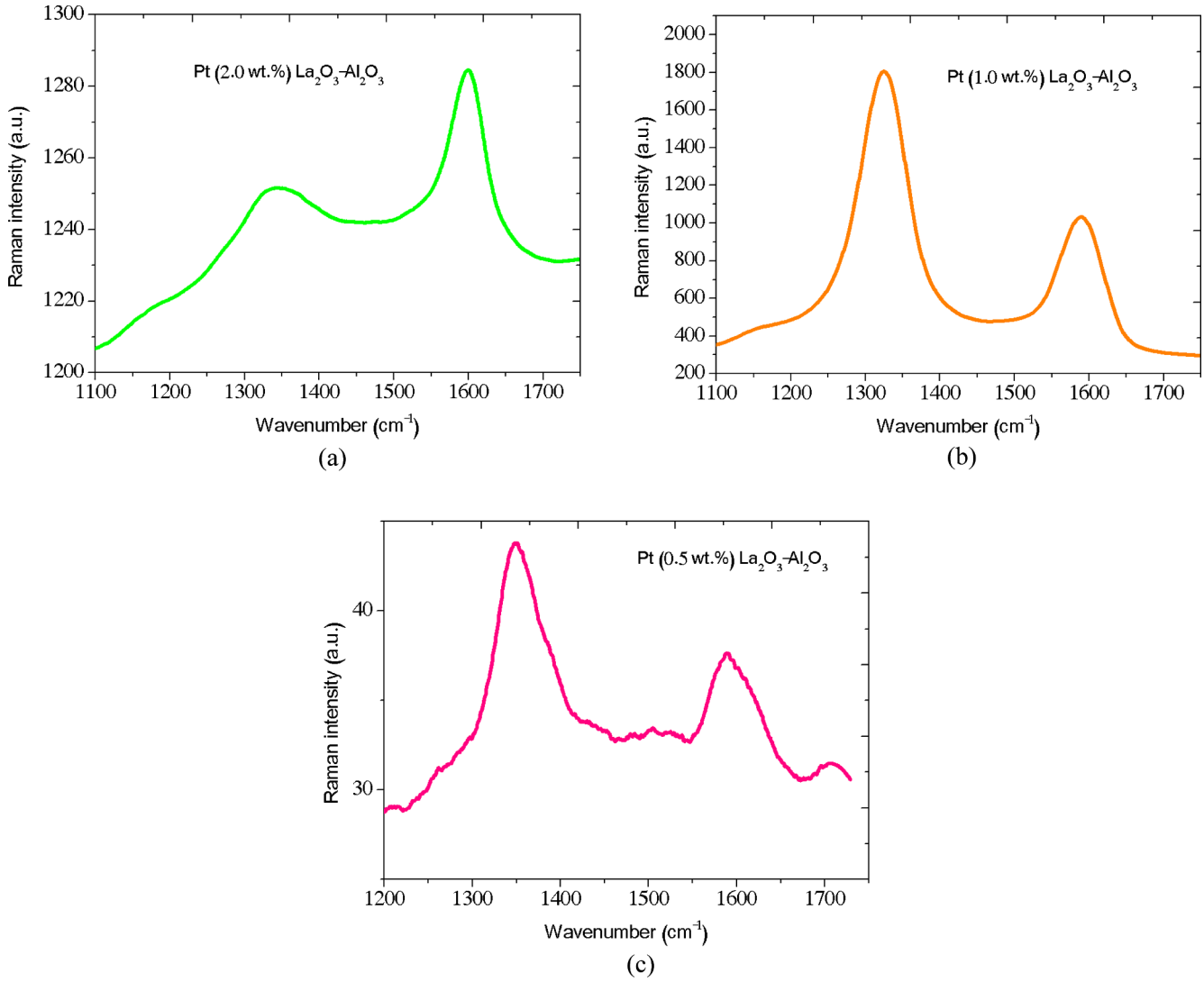


**Fig. 10.** Raman spectra of the spent samples used in POM reaction, (a) Pt(2.0 wt%)/$Al_2O_3$-$La_2O_3$, (b) Pt(1.0 wt%)/$Al_2O_3$-$La_2O_3$ and Pt(0.5 wt%)/$Al_2O_3$-$La_2O_3$.

the G band while the D one is flat (Fig. 10a). This coincides with the fact that the graphite like species is deposited on the solid surface, in line with TEM examinations. It is well known that carbonaceous species are accumulated during the reforming reactions come from $CH_4$ and $CO_2$ molecules [53], regarding the high $CO_2$ selectivity compared with that of hydrogen over Pt(2.0 wt%)/$Al_2O_3$-$La_2O_3$ (Fig. 5b and c). This also illustrates that the CO disproportion to carbon dioxide species is accompanied by carbon formation, which may accumulate on the metallic surface, leading to catalyst deactivation. This agrees with the XPS results that found high carbon content over Pt(2.0 wt%)/$Al_2O_3$-$La_2O_3$ spent catalyst.

Conversely, both Pt(1.0 wt%)/$Al_2O_3$-$La_2O_3$ and Pt(0.5 wt%)/$Al_2O_3$-$La_2O_3$ (Fig. 10b and c) exhibit broader D and G bands and their intensities become significantly higher than that of the 2.0 wt% counterpart. This is accompanied by a notably greater intensity of the D band. Such observations over the catalysts possessing less than 1.0 wt% of Pt are rather expected, particularly considering that their conversions are higher than that of Pt(2.0 wt%)/$Al_2O_3$-$La_2O_3$ (Fig. 5a). Based on this fact, it can be inferred that the amorphous carbon deposition on the metallic Pt particles is chiefly removed by oxygen from the over Pt (0.5 wt%)/$Al_2O_3$ under POM reaction conditions. In addition, the intensity between the D and G band e.g., the $I_D/I_G$ ratio over the Pt(1.0 wt %)/$Al_2O_3$-$La_2O_3$ and Pt(0.5 wt%)/$Al_2O_3$-$La_2O_3$ solids are respectively 0.67 and 0.78. This suggests their better performances, as compared with the Pt(2.0 wt%)/$Al_2O_3$-$La_2O_3$ counterparts ($I_D/I_G$ of ca. 0.81).

Also, these observations account for the deposition of distinct carbon species, which emphasizes that the formation of labile carbon species on the Pt(0.5 wt%)/$Al_2O_3$-$La_2O_3$ impedes the deactivation of this solid. An important point is that the Pt(1.0 wt%)/$Al_2O_3$-$La_2O_3$ exhibits similar Raman features tendencies towards the D and G band, implying in the conclusions drawn before. However, the elevated $CO_2$ selectivity (Fig. 5a) demonstrates that the total combustion of methane reaction is likely over Pt(1.0 wt%)/$Al_2O_3$-$La_2O_3$. Also, the methane decomposition into $CH_x$ species on the surface of Pt particles and its further transformation into carbonaceous deposits lead to a heavy coke accumulation; consequently, a higher degree of catalyst deactivation and Pt particles sintering take place.

From these results, it can be suggested that the catalyst surface reconstructions occur in POM, which ensures stronger interactions between Pt particles and the support, at low Pt loadings as 0.5 wt%. When considering $CH_4$ conversions, lanthana plays an important role of preserving the Pt species dispersion and favoring the reactivity of surface oxygen species of $LaPtO_x[Pt^o]_n$ involved in the surface, at the periphery of $Pt^o$ particles to form $La_2PtO_x[Pt^o]_{n-1}$; thus, the decomposition of $CH_4$ to CO and $H_2$ is likely in the catalysts, as proposed in Fig. 9. The formation of $LaPtO_x[Pt^o]_n$ species on the catalysts surface is reversible and these species would lead to a cleaning of the solid surface via combustion of surface carbon deposits. However, a very low Pt

dispersion provides an enrichment Pt species weakly interacting with the $Al_2O_3$-$La_2O_3$ support, as in the case of Pt loadings superior to 0.5 wt %. This in turn results in the sintering of the particles and deactivation of the solid by coking, as well. On the contrary, a stable performance during POM reaction is observed for 24 h on stream without heavy coke deposition due to the stability of Pt particles, when dispersing a 0.5 wt% of Pt on the support.

## 4. Conclusions

The effect of the Pt loadings is demonstrated via the catalytic performance of the solids during POM and SRM reactions. Low Pt loadings ensured a strong interaction between Pt particles and the $Al_2O_3$-$La_2O_3$ support, which results in high Pt dispersion degree with the participation of lanthana and Pt $[LaPt_xO]Pt^0$ species. Thus, $La_2O_3$ preserved the Pt species with good dispersion and favored the reactivity of surface oxygen species of $LaPtO_x[Pt^o]_n$ involved in the surface, at the periphery of $Pt^o$ particles to form $La_2PtO_x[Pt^o]_{n-1}$. Accordingly, the decomposition of $CH_4$ to CO and $H_2$ and the coke gasification on the accessible Pt sites gave better conversions for Pt(0.5 wt%)/$Al_2O_3$-$La_2O_3$compared with the other solids. At high Pt loadings, however, an enrichment Pt species weakly interacting with the $Al_2O_3$-$La_2O_3$ support caused sintering of the particles and deactivation of the solids by heavy coking. Because of the formation of low reactivity carbon deposits on the Pt surface, the solids possessing more than 0.5 wt% of Pt were not able to alleviate the deactivation during POM and SRM reactions.

## Acknowledgment

This work was supported by the CNPq grant no 406629/2018-8 and Pertobras (“Física do Petróleo em Meios Porosos” Number: F0185). The authors acknowledge the use of the instrumentation facilities of the Central Analítica da Universidade Federal do Ceará and CETENE. FUNCAP and CNPq are thankful acknowledged to the phD scholarships. The authors also would like to acknowledge the assistance of J. L. G. Fierro for XPS analysis. Further assistance for TPR measurements of V. Mortola is also gratefully acknowledged.

## References

[1] Kang D, Lee M, Lim HS, Lee JW. Chemical looping partial oxidation of methane with $CO_2$ utilization on the ceria-enhanced mesoporous $Fe_2O_3$ oxygen carried. Fuel 2018;215:787–98.
[2] Banke K, Hegner R, Schröder D, Schulz C, Atakan B, Kaiser SA. Power and syngas production from partial oxidation of fuel-rich methane/DME mixtures in an HCCI engine. Fuel 2019:24397–5103.
[3] Carvalho DC, de Souza HSA, Filho JM, Oliveira AC, Campos A, Milet ÉRC, et al. A study on the modification of mesoporous mixed oxides supports for dry reforming of methane by Pt or Ru. Appl Catal A: Gen 2014;473:132–45.
[4] Wang A, Austin D, Song H. Investigations of thermochemical upgrading of biomass and its model compounds: opportunities for methane utilization. Fuel 2019:2462443–53.
[5] Yoo J, Bang Y, Han SJ, Park S, Song JH, Song IK. Hydrogen production by tri-reforming of methane over nickel–alumina aerogel catalyst. J Mol Catal A: Chem 2015;410:74–80.
[6] Cui Y, Liu Q, Yao Z, Dou B, Shi Y, Sun Y. comparative study of molybdenum phosphide catalyst for partial oxidation and dry reforming of methane. Int J Hydrogen Energy 2019;44:11441–7.
[7] Meng X, Bi X, Meng B, Yang N, Tan X, Liu L, et al. $H_2/CH_4/CO_2$-tolerant properties of $SrCo_{0.8}Fe_{0.1}Ga_{0.1}O_{3-\delta}$ hollow fiber membrane reactors for methane partial oxidation to syngas. Fuel Process Technol 2017;161:265–72.
[8] Hwan J, Sangbeom S, Jaekyeong Y, Seungwon Y, Min P, Ta YG, et al. The Hydrogen production by steam reforming of ethanol over Ni/$Al_2O_3$-$La_2O_3$ xerogel catalysts. Mol Catal 2017;434:123–33.
[9] Roseno KTC, Schmal M, Brackmann R, Alves RMB. Giudici R, Partial oxidation of methane on neodymium and lanthanium chromate based perovskites for hydrogen production. Int J Hydrogen Energy 2019;41:8166–77.
[10] Chukeaw T, Sringam S, Chareonpanich M, Seubsai A. Screening of single and binary catalysts for oxidative coupling of methane to value-added chemicals. Mol Catal 2019;470:40–7.
[11] Alvarez-Galvan C, Melian M, Ruiz-Matas L, Eslava JL, Navarro RM, Ahmadi M, et al. Partial oxidation of methane to syngas over nickel-based catalysts: influence of support type, addition of rhodium, and preparation method. Front Chem 2019;7:104.
[12] Wei Q, Gao X, Liu G, Yang R, Zhang H, Yang G, et al. Facile one-step synthesis of mesoporous Ni-Mg-Al catalyst for syngas production using coupled methane reforming process. Fuel 2018;211:1–10.
[13] Morala A, Reyero I, Llorca J, Bimbela F, Gandía LM. Partial oxidation of methane to syngas using Co/Mg and Co/Mg-Al oxide supported catalysts. Catal Today 2018. https://doi.org/10.1016/j.cattod.2018.04.003. in press.
[14] Mateos-Pedrero C, Duquesne S, Carrazán SRG, Soria MA, Ruíz P. Influence of the products of the partial oxidation of methane (POM) on the catalytic performances of Rh/Ti-modified support catalysts. Appl Catal A: Gen 2011;394:245–56.
[15] Araujo JCS, Pinheiro ALG, Cruz MGA, Oliveira AC, Bueno JMC, Araujo RS, Lang R. Catalytic assessment of nanostructured Pt/x$La_2O_3$-$Al_2O_3$ oxides for hydrogen production by dry reforming of methane: effects of the lanthana content on the catalytic activity. Catal Today 2018. https://doi.org/10.1016/j.cattod.2018.04.066. in press.
[16] Singh RK, Ghosh S, Acharyya SS, Yadav A, Shukla A, Sasaki T, et al. Partial oxidation of methane to synthesis gas over Pt nanoparticles supported on nanocrystalline $CeO_2$ catalyst. Catal Sci Technol 2016;6:4601.
[17] Al-Sayari SA. Recent developments in the partial oxidation of methane to syngas. Open Catal J 2013;6:17–28.
[18] Araujo JCS, Zanchet D, Rinaldi R, Schuchardt U, Hori CE, Fierro JLG, et al. The effects of $La_2O_3$ on the structural properties of $La_2O_3$–$Al_2O_3$ prepared by the sol–gel method and on the catalytic performance of Pt/$La_2O_3$–$Al_2O_3$ towards steam reforming and partial oxidation of methane. Appl Catal B: Environ 2008:84552–62.
[19] Kang JH, Menard LD, Nuzzo RG, Frenkel AI. Unusual non-bulk properties in nanoscale materials: thermal metal−metal bond contraction of γ-alumina-supported Pt catalysts. J Am Chem Soc 2006;128:12068–9.
[20] Deganello G, Giannici F, Martorana A, Pantaleo G, Prestianni A. Metal-support interaction and redox behavior of Pt (1 wt %)/$Ce_{0.6}Zr_{0.4}O_2$. J Phys Chem B 2006;110:8731–9.
[21] Yang Z, Zhang N, Cao Y, Li Y, Liao Y, Li Y, Gong M, Che Y. Promotional effect of lanthana on the high-temperature thermal stability of Pt/$TiO_2$ sulfur-resistant diesel oxidation catalysts. RSC Adv 2017;7:1931.
[22] Rocha KO, Santos JBO, Meira D, Pizani PS, Marques CMP, Zanchet D, et al. Catalytic partial oxidation and steam reforming of methane on $La_2O_3$–$Al_2O_3$ supported Pt catalysts as observed by X-ray absorption spectroscopy. Appl Catal A: Gen 2012;431–432:79–87.
[23] Zhu Q, Zhao X, Deng Y. Advances in the partial oxidation of methane to synthesis gas. J Natural Gas Chem 2004;13:191–203.
[24] Mortola VB, Damyanova S, Zanchet D, Bueno JMC. Surface and structural features of Pt/$CeO_2$-$La_2O_3$-$Al_2O_3$ catalysts for partial oxidation and steam reforming of methane. Appl Catal B: Environ 2011;107:221–36.
[25] Chen LY, Ni YQ, Zang JL, Lin L, Luo WXH, Cheng S. Structure characterization of platinum/alumina, rhenium/alumina, and platinum-rhenium/alumina catalysts. J Catal 1994;145:132–40.
[26] Lopez T, Villa M, Gomez R. UV-VIs diffuse reflectance spectroscopic study of Pt, Pd, and Ru catalysts supported on silica. J Phys Chem 1991;95:1690–3.
[27] Yang E, Jang EJ, Lee JG, Yoon S, Lee J, Musselwhite N, et al. Acidic effect of porous alumina as supports for Pt nanoparticle catalysts in n-hexane reforming. Catal Sci Technol 2018;8:3295.
[28] Prinetto F, Ghiotti G, Nova I, Lietti L, Tronconi E, Forzatti P. FT-IR and TPD investigation of the $NO_x$ storage properties of BaO/$Al_2O_3$ and Pt-BaO/$Al_2O_3$ catalysts. J Phys Chem B 2001;105:12735.
[29] Resende NS, Perez CA, Eon JG, Schmal M. The effect of coating $TiO_2$ on the CO oxidation of the Pt/c-alumina catalysts. Catal Lett 2011;141:1685–92.
[30] Osmana AI, Abu-Dahrieh JK, Cherkasov N, Fernandez-Garcia J, Walker D, Walton RI, Rooney DW, Rebrov E. A highly active and synergistic Pt/$Mo_2C$/$Al_2O_3$ catalyst for water-gas shift reaction. Mol Catal 2018;455:38–47.
[31] Chen Z, Li J, Yang P, Cheng Z, Li J, Zuo S. Ce-modified mesoporous γ-$Al_2O_3$ supported Pd-Pt nanoparticle catalysts and their structure-function relationship in complete benzene oxidation. Chem Eng J 2019;356:255–61.
[32] Wang P, Yi J, Gu W, Luo P, Lei L. The influence of xMnyCe/c-$Al_2O_3$ on $NO_x$ catalysts on the properties of $NO_x$ storage and reduction over Pt-Ce-Ba/c-$Al_2O_3$ catalysts. Chem Eng J 2017;325:700–7.
[33] Song A, Lu G. Enhancement of Pt–Ru catalytic activity for catalytic wet air oxidation of methylamine via tuning the Ru surface chemical state and dispersion by Pt addition. RSC Adv 2014;4:15325.
[34] Zhang Y, Zhou Y, Wang Q, Shi J, Peng C, He L, Shi L. Manipulating catalytic activity and durability of Pt-modified Cu–Fe–La/γ-$Al_2O_3$ ternary catalyst for catalytic wet air oxidation: effect of calcination temperature. RSC Adv 2018;8:547.
[35] Wang H, Dong J, Allard LF, Leed S, Oh S, Wang J, et al. Single-site Pt/La-$Al_2O_3$ stabilized by barium as an active and stable catalyst in purifying CO and $_C3_H6$ emissions. Appl Catal B: Environ 2019;244:327–39.
[36] Moraes TS, Neto RCR, Ribeiro MC, Mattos LV, Kourtelesis M, Ladas S, Verykios X, Noronha FB. Ethanol conversion at low temperature over $CeO_2$—Supported Ni-based catalysts. Effect of Pt addition to Ni catalyst. Appl Catal B: Environ 2016;181:754–68.
[37] Ruiz-Vizcaya ME, Novaro O, Ferreira JM, Gomez R. Determination of the mechanism of cyclohexane dehydrogenation over Pt- and Pt-Pd-supported catalysts through theoretical and experimental studies. J Catal 1978;51:108–14.
[38] Feio LSF, Hori CE, Damyanova S, Noronha FB, Cassinelli WH, Marques CMP, et al. The effect of ceria content on the properties of Pd/$CeO_2$/$Al_2O_3$ catalysts for steam reforming of methane. Appl Catal A: Gen 2007;316:107–16.
[39] Wei J, Iglesia E. Structural requirements and reaction pathways in methane activation and chemical conversion catalyzed by rhodium. J Catal 2004;225:116–27.
[40] Rameshan C, Li H, Ani K, Roiaz M, Pramhaas V, Rameshan R, et al. In situ NAP-XPS

spectroscopy during methane dry reforming on $ZrO_2$/Pt(111) inverse model catalyst. J Phys: Condens Matter 2018;30:264007.
[41] Coelho DC, Oliveira AC, Filho JM, Oliveira AC, Lucredio AF, Assaf EM, et al. Effect of the active metal on the catalytic activity of the titanate nanotubes for dry reforming of methane. Chem Eng J 2016;290:438–53.
[42] Wolfbeisser A, Klötzer B, Mayr L, Rameshan R, Zemlyanov D, Bernardi J, et al. Surface modification processes during methane decomposition on Cu-promoted Ni–$ZrO_2$ catalysts. Catal Sci Technol 2015;5:967–78.
[43] Ochoa A, Aramburu B, IbµÇez M, Valle B, Bilbao J, Gayubo AG, et al. Compositional insights and valorization pathways for carbonaceous material deposited during bio-oil thermal treatment. ChemSusChem 2014;7:2597–608.
[44] Bezerra DP, Azevedo DCS, Pinheiro LG, Filho JM, Oliveira AC. Production of α, β-unsaturated esters via Knoevenagel condensation of buthyraldehyde and ethyl cyanoacetate over amine-containing carbon catalyst. Chem Eng J 2015;264:565–656.
[45] Tao FF, Shan J-J, Nguyen L, Wang Z, Zhang S, Zhang L, et al. Understanding complete oxidation of methane on spinel oxides at a molecular level. Nat Comm 2015;6:7798.
[46] Fina F, Menard H, Irvine JTS. The effect of Pt NPs crystallinity and distribution on the photocatalytic activity of Pt–g-$C_3N_4$. Phys Chem Chem Phys 2015;17:13929.
[47] Wei Q, Yang G, Yoneyama Y, Vitidsant T, Tsubaki N. Designing a novel Ni–$Al_2O_3$–SiC catalyst with a stereo structure for the combined methane conversion process to effectively produce syngas. Catal Today 2016;265:36–44.
[48] Liu T, Snyder C, Veser G. Catalytic partial oxidation of methane: is a distinction between direct and indirect pathways meaningful? Ind Eng Chem Res 2007;46:9045–52.
[49] Xu X, Tang W, Zhou Y, Bao Z, Su Y, Hu J, et al. Steering photoelectrons excited in carbon dots into platinum cluster catalyst for solar-driven hydrogen production. Adv Sci 2017;4:1700273.
[50] Fleisch TH, Hicks RF, Bell A. An XPS study of metal-support interactions on Pd/$SiO_2$ and Pd/$La_2O_3$. J Catal 1984;87(2):398–413.
[51] Chin Y-H, Buda C, Neurock M, Iglesia E. Selectivity of chemisorbed oxygen in C-H bond activation and CO oxidation and kinetic consequences for $CH_4$–$O_2$ catalysis on Pt and Rh clusters. J Catal 2011;283:10–24.
[52] Sousa FF, Sousa HSA, Oliveira AC, Junior MCC, Ayala AP, Barros EB, et al. Nanostructured Ni-containing spinel oxides for the dry reforming of methane: effect of the presence of cobalt and nickel on the deactivation behaviour of catalysts. Int J Hydrogen Energy 2012;37:3201–12.
[53] Korup O, Schlögl R, Horn R. Carbon formation in catalytic partial oxidation of methane on platinum: model studies on a polycrystalline Pt foil. Catal Today 2012;181:177–83.
[54] Efstathiou AM, Kladi A, Tsipouriari VA, Verykios XE. Reforming of methane with carbon dioxide to synthesis gas over supported rhodium catalysts. J Catal 1996;158:64–75.